


Article

# Numerical Study of Effects of Winds and Tides on Monthly-Mean Circulation and Hydrography over the Southwestern Scotian Shelf

Qiantong Pei \*, Jinyu Sheng \* and Kyoko Ohashi 

Department of Oceanography, Dalhousie University, Halifax, NS B3H 4R2, Canada

\* Correspondence: qn317878@dal.ca (Q.P.); jinyu.sheng@dal.ca (J.S.)

**Abstract:** A nested-grid modelling system is used to quantify effects of winds and tides on the three-dimensional (3D) circulation and hydrography over the southwestern Scotian Shelf (swScS) and surrounding areas in 2018. The performance of the nested-grid modelling system is assessed by comparing model results with observations and reanalysis data. Analysis of model results demonstrates that both winds and tides enhance the vertical mixing and modify the 3D circulation over the swScS. In winter (summer), the wind-induced vertical mixing warms (significantly cools) the sea surface temperature (SST) over the Scotian Shelf (ScS). In addition to intense vertical mixing associated with winter convection, the wind-induced mixing raises the sea surface salinity (SSS) by entraining the relatively salty sub-surface waters with the surface waters. The effect of wind-induced vertical mixing is evident in the upper water columns of ~40 m (~15 m) in February (August) 2018 over the swScS, reflecting the typically stronger wind forcing in winter than in summer. The wind forcing also enhances the seaward spreading of river runoff. Strong tidal mixing and advection also play an important role in affecting the hydrography and density-driven currents over the Bay of Fundy (BoF), Georges Bank (GeB), and swScS. In summer, tides significantly reduce the SST, increase the SSS, and affect large density-driven currents over the BoF, GeB, and swScS. Winds and tides also modify the large-scale ocean circulation, eddies, meanders, and frontal structures in the deep waters off the swScS through the modulation of baroclinic hydrodynamics.

**Keywords:** winds; tides; circulation; coastal upwelling; scotian shelf; nested-grid model



**Citation:** Pei, Q.; Sheng, J.; Ohashi, K. Numerical Study of Effects of Winds and Tides on Monthly-Mean Circulation and Hydrography over the Southwestern Scotian Shelf. *J. Mar. Sci. Eng.* **2022**, *10*, 1706. <https://doi.org/10.3390/jmse10111706>

Academic Editor: Vengatesan Venugopal

Received: 23 September 2022

Accepted: 3 November 2022

Published: 9 November 2022

**Publisher's Note:** MDPI stays neutral with regard to jurisdictional claims in published maps and institutional affiliations.



**Copyright:** © 2022 by the authors. Licensee MDPI, Basel, Switzerland. This article is an open access article distributed under the terms and conditions of the Creative Commons Attribution (CC BY) license (<https://creativecommons.org/licenses/by/4.0/>).

## 1. Introduction

The Scotian Shelf (ScS; see Appendix A for a list of abbreviations) is a rugged open shelf off Nova Scotia, Canada, bounded by the Northeast Channel, Laurentian Channel, and deep waters of the northwest North Atlantic Ocean (Figure 1a). The ScS is about 700 km long and has a width varying from 160 to 240 km, with an average depth of about 90 m [1,2]. There are three main sources for the waters over the ScS: the Labrador Current, the outflow from the Gulf of St. Lawrence (GSL) at the upstream (northeast) end of the Shelf, and North Atlantic water from offshore [1]. Hydrodynamics over the ScS have large temporal and spatial variability and are significantly affected by atmospheric and tidal forcing.

Circulation and hydrography over the ScS have been the subject of many previous studies. Smith et al. [1] demonstrated that the role of winds in the alongshore dynamic balance differs between the inshore and offshore regions of the ScS. Schwing [3,4] demonstrated that the time-varying local winds strongly affect the temporal variability of three-dimensional (3D) circulation over the ScS. The numerical study of Greenberg et al. [5] indicated that the barotropic response is an important part of the oceanic response to winds over the ScS and Gulf of Maine (GoM), and the alongshore winds are more effective in forcing the barotropic response over the ScS and GoM than the cross-shore winds. Zhai et al. [6] described a strong baroclinic throughflow with variations on the O(days) scale associated with winds

over the deep waters outside Lunenburg Bay. Shan and Sheng [7] recently investigated the important role of wind impulses during coastal upwelling events over the ScS.

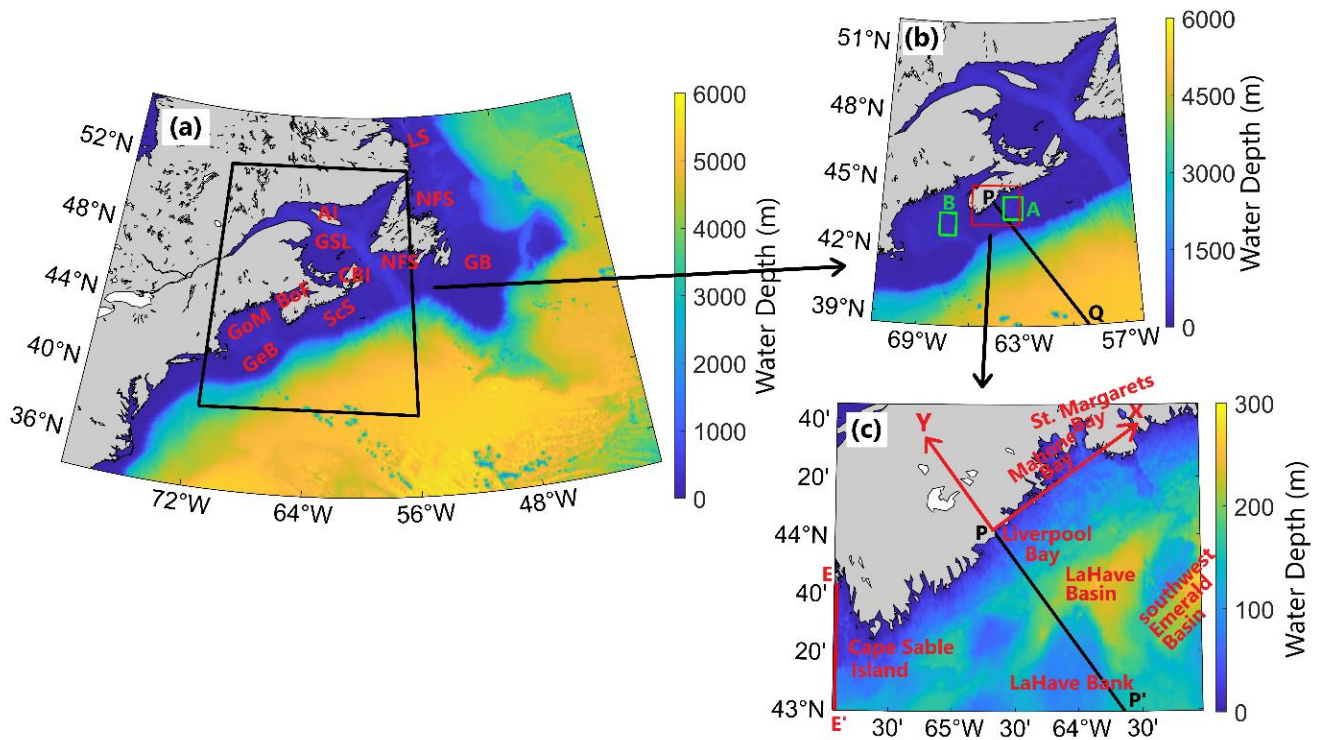


**Figure 1.** Major geographic features and domains of the three submodels composing the nested-grid coupled circulation-ice modelling system (NGMS-seCS) for the southeastern Canadian shelf and adjacent deep ocean waters of the northwest Atlantic Ocean. The horizontal resolutions of submodels (a) L1, (b) L2, and (c) L3 are  $1/12^\circ$ ,  $1/36^\circ$ , and  $1/108^\circ$ , respectively. The color image in each subplot represents water depths. Transect PP' is a cross-shelf transect originating from Liverpool Bay. Transect PQ is the extension of transect PP' over the L2 domain. Transect EE' is a north-south transect originating from Yarmouth, which is close to the western open boundary of submodel L3. Figure 1c shows the coordinate system for the transects PP' and PQ. Definitions of abbreviations are given in Appendix A. Green boxes A and B are in the swScS and central GoM, respectively, over which the time series of simulated SST are compared with the satellite remote sensing observations.

Tidal sea levels or/and tidal currents are large over certain coastal and shelf waters, such as the Bay of Fundy (BoF) and Georges Bank (GeB), of the southeastern Canadian shelf (seCS; Figure 1a) and are relatively weak in the adjacent deep ocean. Large tidal currents and tidal mixing modify the general mean circulation and hydrography over coastal and shelf waters, resulting in significant modulations of density-driven currents and baroclinic hydrodynamics. Smith et al. [1] found that the semidiurnal  $M_2$  constituent is the dominant tidal component on the ScS, and the generation of  $M_2$  baroclinic tides over the shelf break leads to internal Reynolds stress divergences (comparable to the geostrophic terms) that are capable of providing significant contribution to the mean momentum balance. Tidal rectification, on the other hand, supports the anticyclonic gyre around Browns Bank and induces the westward and offshore near-bottom currents off Cape Sable [8]. Based on 3D model results, Wang et al. [9] demonstrated that tidal impacts are relatively small over the Labrador Shelf (LS), Newfoundland Shelf (NFS) and Grand Banks (GB), moderate over the ScS, and large over the central and eastern GoM, the upper BoF, and the northern flank of GeB. Previous studies also demonstrated that tides are of great importance to near-bottom currents, particularly over some shallow areas over the ScS, and thus generates important local hydrodynamical phenomena [8,10–12].

The above and other previous studies have indicated that both winds and tides play important roles in the temporal and spatial variability of circulation and hydrography over the ScS. Several important scientific questions remain to be investigated, such as what the effects of winds are on the hydrography and circulation over the inner ScS, and what the major impacts of tidal forcing are on the hydrography and circulation over the southwestern ScS (swScS). In this study, we address these questions based on analyses of model results produced by a three-level nested-grid circulation-ice modelling system for the seCS. A process study is conducted using this modelling system to quantify the roles of winds and tides in the temporal and spatial variability of the 3D hydrography and circulation over the swScS. The accumulative effects of wind and tidal forcing are examined based on analyses of model results in three numerical experiments using different combinations of external forcings.

This paper is structured as follows. Section 2 introduces the nested-grid coupled circulation-ice modelling system and external forcing. In Section 3, results of the coupled modelling system are validated against available observations and reanalysis data. In Section 4, a process study with three numerical experiments is conducted to examine the effects of wind and tidal forcing, with a specific focus on the hydrodynamics over the swScS. Section 5 provides a summary and conclusions.

## 2. Materials and Methods

### 2.1. Nested-Grid Coupled Circulation-Ice Modelling System

The nested-grid circulation-ice modelling system (hereinafter NGMS-seCS) used in this study is based on the Regional Ocean Modelling System (ROMS; [13]; [myroms.org](https://myroms.org) (accessed on 1 November 2022)) and Los Alamos Sea Ice Model (CICE; [14]; [zenodo.org/record/1205674](https://zenodo.org/record/1205674) (accessed on 1 November 2022)). The ROMS is a free-surface and terrain-following numerical ocean model, which numerically solves the Reynolds-averaged Navier-Stokes equations with hydrostatic and Boussinesq assumptions. The CICE is a numerical model for simulating the growth, melting, and movement of sea ice. It numerically solves two main physics equations for the sea ice: (a) Newton's second law for sea ice and (b) the evolution of the sea ice thickness distribution for different thicknesses spread of the area [14]. An external coupler ([github.com/kshedstrom/roms](https://github.com/kshedstrom/roms) (accessed on 1 November 2022)) is used for two-way coupling between ROMS and CICE. The bathymetry of the coupled modelling system is based on the GEBCO\_2014 dataset ([gebcو.net/data\\_and\\_products/gebcو\\_web\\_services](https://gebcو.net/data_and_products/gebcو_web_services) (accessed on 1 November 2022)).

The NGMS-seCS has three submodels, with nested domains of successively smaller areas and higher horizontal resolutions. The domain of submodel L1 covers the seCS and adjacent deep ocean waters between 80° W and 40° W, and between 34° N and 55° N (Figure 1a), with a horizontal resolution of 1/12°. The domain of submodel L2 covers the Gulf of St. Lawrence-Scotian Shelf-Gulf of Maine (GSL-ScS-GoM) region, and adjacent deep waters between 71.5° W and 56° W and 38.5° N and 52° N (Figure 1b), with a horizontal resolution of 1/36°. The domain of submodel L3 covers the swScS between 66.0° W and 63.0° W and 43° N and 44.75° N (Figure 1c), with a horizontal resolution of 1/108° (~730 m).

A one-way nesting technique is used in the NGMS-seCS, in which information from the upper-level submodel is transferred to the lower-level submodel. Specifically, simulated values of sea levels, currents, temperature, salinity, and sea ice conditions produced by the parent model are used to specify lateral boundary conditions for the child model. In each submodel, the Smagorinsky scheme [15] and the level 2.5 Mellor-Yamada turbulence closure scheme [16] are used for the horizontal and vertical eddy mixing coefficients, respectively. The logarithmic parameterization is used for the bottom friction (Appendix B). Each submodel has 40 terrain-following layers in the vertical, in which the layers are concentrated near the surface in deep waters and more uniformly distributed in shallow waters.

## 2.2. Initial Conditions and External Forcing

The model's initial conditions of temperature, salinity, sea level, and 3D currents are based on the daily mean Global Ocean Physics Reanalysis dataset (GLORYS 12V1) which has a horizontal resolution of  $1/12^\circ$ . This dataset was constructed by the Copernicus—Marine Environment Monitoring Service (CMEMS; [resources.marine.copernicus.eu](https://resources.marine.copernicus.eu), accessed on 5 October 2022).

The NGMS-seCS is driven by tides, atmospheric forcing, freshwater discharge, and boundary forcing specified at the lateral open boundaries. Tides are specified at the open boundaries of the outer-most submodel (L1) in terms of tidal sea levels and depth-mean currents of 11 major tidal constituents ( $M_2$ ,  $S_2$ ,  $N_2$ ,  $K_2$ ,  $K_1$ ,  $O_1$ ,  $P_1$ ,  $Q_1$ ,  $M_4$ ,  $MS_4$ , and  $MN_4$ ). The harmonic constants of these tidal constituents were extracted from the regional solution for the Atlantic Ocean of the Oregon State University Tidal Inversion System (OTIS; [17]; [www.tpxo.net/otis](http://www.tpxo.net/otis) (accessed on 1 November 2022)), which has a horizontal resolution of  $1/12^\circ$ .

The atmospheric forcing used to drive the NGMS-seCS includes the three-hourly fields of air pressure, specific humidity, and air temperature at or near the sea surface, and wind velocity at 10 m above the mean sea level. These fields were extracted from the three-hourly North American Regional Reanalysis (NARR; [18]), which has a horizontal resolution of 32 km. The bulk formula by Large and Pond [19] is used to calculate the wind stress from the wind velocity. The atmospheric forcing also includes three-hourly shortwave and longwave radiation fluxes, cloud fraction, and precipitation.

Freshwater discharges from 49 major rivers over the seCS are specified in the NGMS-seCS using the monthly-mean climatological data described by Lin et al. [20], except for the St. Lawrence River (SLR), the discharge of which is derived from monthly-mean values estimated with the regression model by Bourgault and Koutitonsky [21] and published by the St. Lawrence Global Observatory ([slgo.ca](http://slgo.ca) (accessed on 1 March 2019)). The freshwater discharge from each river is specified at the head of an idealized channel cut into the coastline, using the river scheme developed by Sheng et al. [22] and Ji et al. [23].

In submodel L1, the lateral open boundary conditions of model variables are derived from the daily GLORYS 12V1 dataset. The adaptive open boundary condition of Marchesiello et al. [24] is used in submodel L1, with time scales of 1 day for inward flux and 360 days for outward flux. At each lateral open boundary, a “sponge” layer is defined in which the simulated temperature and salinity are nudged towards daily-mean reanalysis values. The configuration of these layers is described in Appendix C.

In submodels L1 and L2, the semi-prognostic method developed by Sheng et al. [25] and the spectral nudging method developed by Thompson et al. [26] are used to reduce the systematic bias and seasonal drift in the model. In this study, the coefficient for the semi-prognostic method is set to 0.15. The spectral nudging method is only applied at depths below 30 m, to allow model hydrography near the sea surface to be prognostic. The spectral nudging coefficient linearly increases from 0 to 0.0011 between 30 and 40 m and is 0.0011 at depths greater than 40 m. The semi-prognostic and spectral nudging methods are described in Appendices D and E, respectively.

## 2.3. Numerical Experiments

Model results from three numerical experiments (Table 1) with different external forcings for 2018 are examined to quantify the effects of winds and tides on monthly-mean temperature, salinity, and circulation over the swScS. The first numerical experiment is the Control Run (case CR), in which the NGMS-seCS is driven by all external forcing discussed above, including tides, winds, atmospheric pressure, net heat and freshwater fluxes at the sea surface, and river discharge. The second numerical experiment (case NW) is the same as the Control Run except for the exclusion of winds in both submodels L2 and L3 (Figure 1b,c). The third numerical experiment is case NT, which is the same as case CR except for the exclusion of tidal forcing.

**Table 1.** List of four numerical experiments using the NGMS-seCS.

Numerical Experiment	Tidal Forcing	Wind Forcing in Submodel L2	Wind Forcing in Submodel L3	Other Forcing
CR	Yes	Yes	Yes	Yes
NW	Yes	No	No	Yes
NT	No	Yes	Yes	Yes

Model results in cases CR and NW are compared to examine the effects of winds on hydrography and currents over the swScS. It should be noted that the latent and sensible heat fluxes are proportional to wind speeds, resulting in the absence of the latent and sensible heat fluxes in case NW. Since these numerical experiments are used to investigate the effects of winds and tides over coastal and shelf waters, both the semi-prognostic method by Sheng et al. [25] and the spectral nudging method by Thompson et al. [26] are used in submodels L1 and L2 to reduce model bias and drift in the seasonal cycle and large-scale circulation.

### 3. Model Results and Validation

The NGMS-seCS was integrated for the year from 1 January 2018 to 31 December 2018. The performance of submodel L1 in simulating the sea level, sea surface temperature (SST), and sea surface salinity (SSS) was assessed in this section by comparing model results in case CR with in situ oceanographic observations provided by the Marine Environmental Data Service of Fisheries and Oceans Canada (MEDS-DFO; [isdm-gdsi.gc.ca](http://isdm-gdsi.gc.ca) (accessed on 1 November 2022)) and satellite remote sensing data. Performance of the sea ice model is evaluated in Appendix F.

#### 3.1. Sea Levels

Tide gauge data at Halifax, obtained from the MEDS-DFO, were used to assess the performance of submodel L1 in simulating sea level. Figure 2a presents the time series of observed and simulated total sea levels at Halifax for the period from 5 February 2018 to 27 March 2018. This period was chosen because the wind forcing is typically strong during this time of year, which allows us to evaluate the model's performance in simulating both tidal and sub-tidal levels. The value of  $\gamma^2$  (defined in Appendix G) for simulating the total sea level is  $\sim 0.09$  for this period, and the model has a similar performance (with  $\gamma^2$  in the same order of magnitudes) in simulating total sea levels for other periods in 2018. This indicates the satisfactory performance of submodel L1 in simulating the total sea levels at Halifax.

The total sea level is affected by both tidal and non-tidal forcing. To examine the model's response to these two types of forcings, the observed and simulated total sea levels were decomposed into tidal and non-tidal components using the tidal analysis package `t_tide` [27]. Because the non-tidal levels obtained from `t_tide` still have some tidal components, remaining high-frequency variability with periods of less than 3 h is removed with a low-passed filter. Figure 2b demonstrates that submodel L1 performs very well in simulating tidal sea levels in Halifax, with a  $\gamma^2$  value of  $\sim 0.04$ .

The  $\gamma^2$  value for simulating the non-tidal level (Figure 2c) is  $\sim 0.304$ , which is larger than the  $\gamma^2$  value for the tidal sea levels. One plausible reason is that the relevant atmospheric variables (i.e., winds and atmospheric pressures) over coastal waters near Halifax, particularly during storm events, are not well represented by the NARR products, which have a horizontal resolution of  $O(10\text{ km})$ . Another plausible reason is the absence of wave-current interactions in the NGMS-seCS. Under strong wind conditions (particularly during extreme weather events), wave-current interactions affect the accuracy of simulated sea levels [20,28]. In addition, the parameterizations of sub-grid mixing, i.e., the Smagorinsky scheme and level 2.5 Mellor-Yamada turbulence closure, and bottom friction,

i.e., the logarithmic parameterization with  $z_0 = 0.02$  m [29], also affect the model accuracy in simulating sub-tidal sea levels.

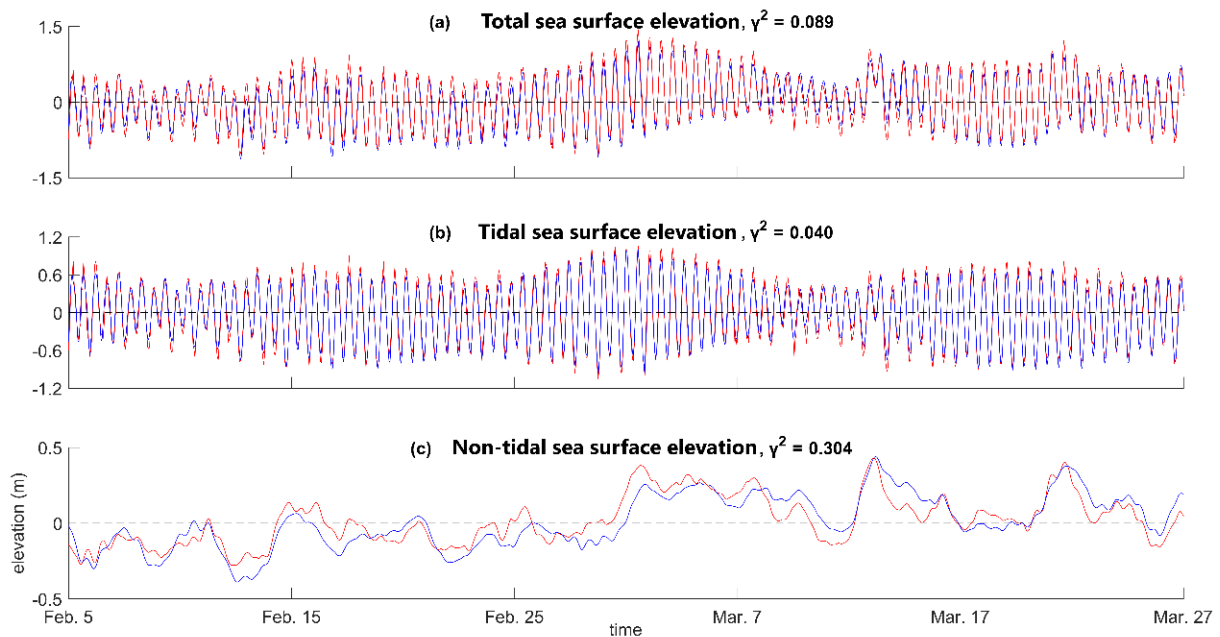


**Figure 2.** Time series of observed (red) and simulated (blue) (a) total, (b) tidal, and (c) non-tidal sea levels at Halifax for the period from 5 February to 27 March 2018. The simulated results are produced by submodel L1.

Although larger than the value for the tidal sea levels, the  $\gamma^2$  value for the non-tidal sea levels is comparable to those in past studies [30], indicating that submodel L1 has reasonable skills in reproducing the non-tidal levels over coastal waters of the ScS. At other tidal gauge stations (e.g., Yarmouth, North Sydney, Charlottetown) and during other time periods in 2018, submodel L1 also performs well in simulating the tidal and non-tidal sea levels, with values of  $\gamma^2$  in the same order of magnitude as at Halifax (Table 2).

**Table 2.** List of  $\gamma^2$  values for total, tidal, and sub-tidal surface elevations.

Stations	Total	Tidal	Sub-Tidal
Halifax	0.089	0.040	0.304
Yarmouth	0.023	0.013	0.318
Charlottetown	0.031	0.017	0.298
Port aux basques	0.054	0.030	0.336
North Sydney	0.067	0.044	0.166

To further assess the model performance in reproducing tidal sea levels over the seCS, tidal harmonic analyses using  $t\_tide$  were conducted to determine amplitudes and phases of the  $M_2$  and  $K_1$  sea levels from hourly results produced by submodel L1 during the period 1–30 June 2018 (Figure 3a,c). The co-phases and co-amplitudes of the  $M_2$  and  $K_1$  sea levels from the OTIS tidal model solution (source of the tidal forcing for submodel L1) are presented respectively in Figure 3b,d. The OTIS is one of the best products for barotropic tides in the global oceans, since it assimilates various satellite altimetric data and in situ observations into the tidal circulation model. Figure 3a,b demonstrates that submodel L1 reproduces reasonably well the distributions of co-amplitudes and co-phases of  $M_2$  tidal sea levels over the seCS and adjacent deep waters. In particular, submodel L1 reproduces reasonably well the positions of two  $M_2$  amphidromic points, with one close to the eastern boundary of the L1 domain and the other in the middle of the GSL. Around

both amphidromic points, the  $M_2$  tidal waves cyclonically rotate. The amplitudes of  $M_2$  sea levels (Figure 3a,b) are large in the St. Lawrence Estuary (SLE), the BoF, and the GoM. In the SLE, the maximum amplitudes of the  $M_2$  sea levels exceed 1.5 m. In the GoM, the amplitudes of the  $M_2$  sea levels are generally more than 0.7 m and decrease to less than 0.5 m over GeB and adjacent deep waters. In the BoF, the amplitudes of  $M_2$  tidal sea levels are generally more than 4.0 m. Over the ScS and southern NFS, the amplitudes of the  $M_2$  tidal sea levels are generally between 0.4 and 0.6 m. The positions of  $M_2$  amphidromic points, rotations of  $M_2$  tides, and distributions of  $M_2$  co-amplitude produced by submodel L1 also agree with previous model results obtained by Han et al. [31] and Wang et al. [9]. The  $M_2$  co-phases calculated from the NGMS-seCS results, such as the 210-degree-contour, feature some oscillations absent in the OTIS results. These oscillations are mainly due to model-simulated baroclinic hydrodynamics, with contributions from model artefacts.

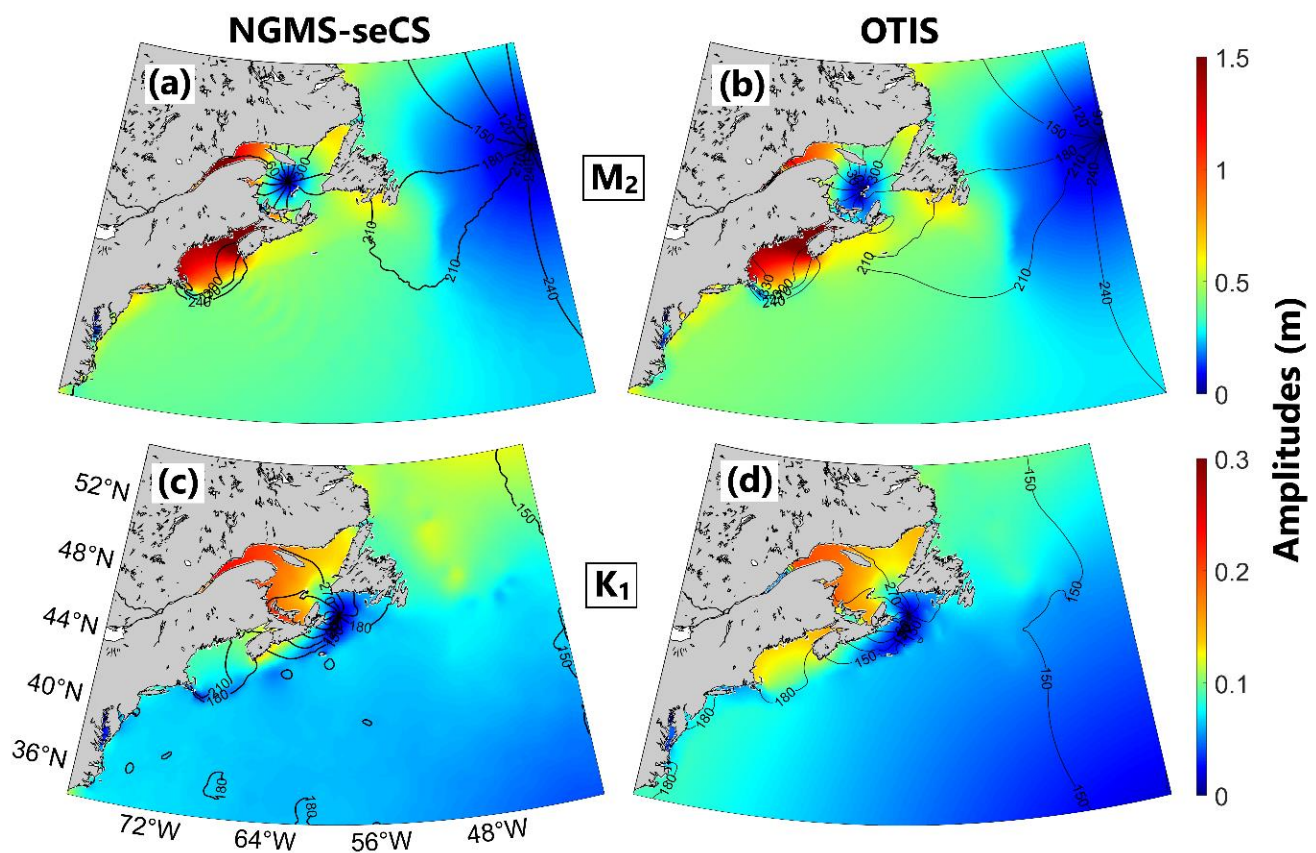


**Figure 3.** Co-phases (black contour lines) and co-amplitudes (color image) of the  $M_2$  (a,b) and  $K_1$  (c,d) tidal sea levels simulated by submodel L1 (a,c), and from the OTIS regional tidal model solution (b,d).

Submodel L1 also has reasonable skills in reproducing distributions of co-phases and co-amplitudes of  $K_1$  sea levels over the GSL, ScS, and GoM (Figure 3c,d). The model reasonably reproduces the position of the  $K_1$  amphidromic point over the southern Laurentian Channel. Around the  $K_1$  amphidromic point, the  $K_1$  tidal waves cyclonically rotate. The simulated position of this amphidromic point and the cyclonic rotation of  $K_1$  sea levels are generally consistent with the OTIS model results and other previous studies (e.g., Han et al. [31]; Wang et al. [9]). Some small-scale differences occur in co-phases and co-amplitudes of the  $K_1$  sea levels between our model results and OTIS over deep waters (Figure 3c,d). One possible explanation is baroclinic hydrodynamics and other physical processes over the deep ocean. Submodel L1 generates small-scale features in co-amplitudes and co-phases in the deep ocean waters to the south of the ScS and GoM, mainly due to baroclinic dynamics (Wang et al. [9]). The marked differences in the  $K_1$

co-phases and co-amplitudes in the GoM between the NGMS-seCS and OTIS (Figure 3c,d) results are mainly associated with the  $K_1$  component of the baroclinic tides.

### 3.2. Surface Tidal Currents

The surface  $M_2$  tidal current ellipses in June 2018 over the GSL-ScS-GoM (Figure 4a) are calculated from the hourly model results produced by submodel L2 in case CR using  $t_{\text{tide}}$ . The surface  $M_2$  tidal current ellipses in this month have considerable spatial variability over the L2 domain, with the strongest  $M_2$  surface currents ( $>1 \text{ m}\cdot\text{s}^{-1}$ ) in the BoF, mainly due to the resonant characteristics of  $M_2$  tides over the area [32]. Large  $M_2$  surface currents also occur over the swScS and the southern flank of GeB, with the major axes of the  $M_2$  current ellipses normal to the local isobaths. In the BoF, southern flank of GeB, and coastal waters of the swScS, the surface  $M_2$  current ellipses produced by the NGMS-seCS are generally comparable with their counterparts from Wang et al. [9] (Figure 4b), in terms of both the magnitudes and directions of the surface  $M_2$  currents. Relatively strong surface  $M_2$  currents occur over the outer shelf of the ScS (Figure 4a), which agree well with the results of Ohashi et al. [32] and Wang et al. [9]. The surface  $M_2$  currents gradually decrease from the southern flank of southeastern GeB to the deep waters off the swScS, which is consistent with the results of Katavouta et al. [33] and Wang et al. [9]. Over Northumberland Strait (southwestern GSL), submodel L2 is able to reproduce the strong rectilinear surface  $M_2$  currents, which are highly comparable with the results of Ohashi et al. [32]. The surface  $M_2$  currents are weak in the rest of the deep waters (beyond the 1000 m isobaths plotted in green in Figure 4a) over the L2 domain.

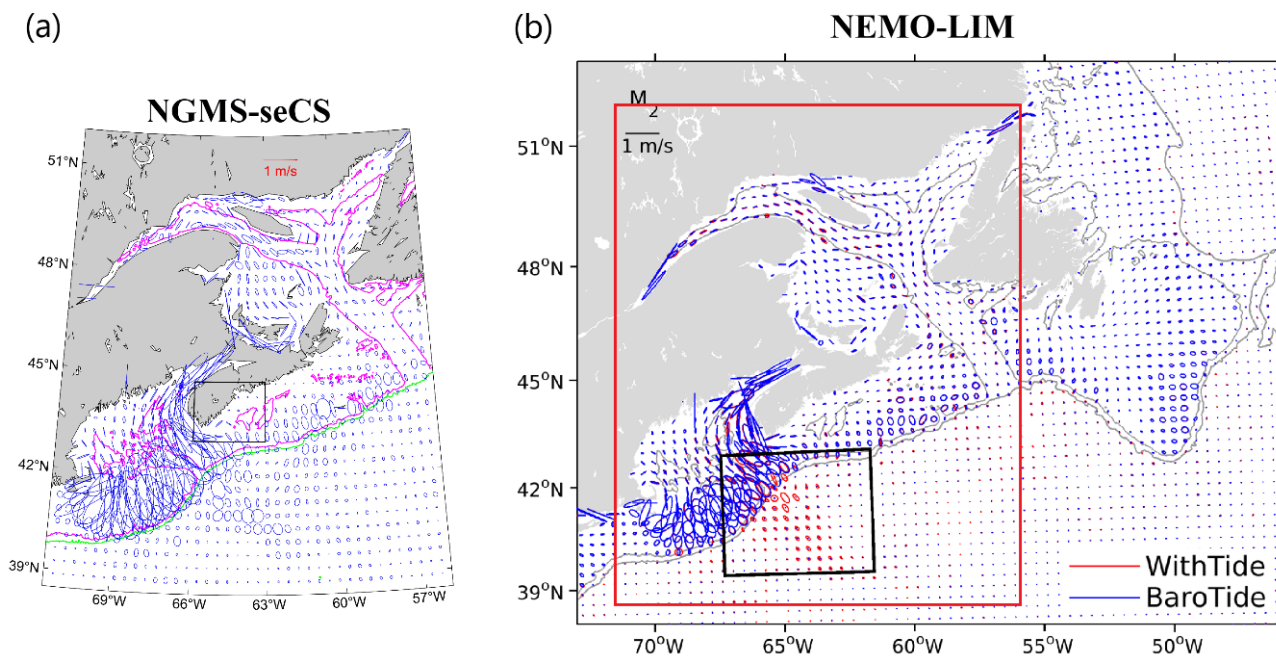


**Figure 4.** (a) Ellipses of (a) surface  $M_2$  tidal currents (blue ellipses) for June 2018 simulated in case CR and (b) the counterparts taken from Wang et al. [9] (red ellipses represent baroclinic  $M_2$  tides and blue ellipses represent barotropic  $M_2$  tides). For clarity, the  $M_2$  tidal current ellipses in (a) are plotted at every 14th grid point of submodel L2. The ellipses inside (outside) the black box in (a) are based on results of submodel L3 (submodel L2). The magenta and green contours represent the 200-m and 1000-m isobaths, respectively. The red box in (b) indicates the L2 domain of the NGMS-seCS.

It should be noted that the surface  $M_2$  tidal current ellipses shown in Figure 4a are calculated based on the baroclinic tidal currents at the sea surface in June 2018, which is different from the simulation period of Wang et al. [9]. Therefore, the baroclinic tidal currents (and baroclinic hydrodynamics) generated by submodel L2 can differ from the counterparts from Wang et al. [9] over some local areas due to the temporal variability of



baroclinic tidal currents. Furthermore, submodel L2 uses the sigma-level, with a higher horizontal resolution ( $1/36^\circ$ ) than the numerical model ( $1/12^\circ$ ) used by Wang et al. [9]. As a result, submodel L2 resolves more fine-scale topographic features than the numerical model used by Wang et al. [9]). These fine-scale topographic features affect the small- and meso-scale baroclinic hydrodynamics over coastal and shelf waters, consequently contributing to the noticeable differences in surface  $M_2$  tidal current ellipses between Figure 4a,b.

### 3.3. Sea Surface Temperature and Salinity

We next assess the performance of the NGMS-seCS in simulating the monthly-mean SST and SSS by comparing model results with the satellite remote sensing data. The SST satellite remote sensing data used here were extracted from the daily GHRSSST Level 4 CMC0.1deg Global Foundation Sea Surface Temperature Analysis (GDS version 2) dataset, provided by the Physical Oceanography Distributed Active Archive Center (PODAAC). This dataset was constructed by merging the infrared satellite SSTs from the Advanced Very High Resolution Radiometers (NOAA-18, NOAA-19, METOP-A, and METOP-B) and microwave SST data from the Advanced Microwave Scanning Radiometer 2 onboard the GCOM-W satellite in conjunction with in situ observations of SST from drifting buoys and ships from the ICOADS program ([icoads.noaa.gov](http://icoads.noaa.gov) (accessed on 1 November, 2022)). The SSS remote sensing data were extracted from the Sea Surface Salinity Essential Climate Variable (ECV) dataset (version 1.8) produced by the European Space Agency's (ESA) Climate Change Initiative (CCI).

The simulated monthly-mean SST in March 2018 (Figure 5a) is relatively cool and ranges from  $-2^\circ\text{C}$  to  $5^\circ\text{C}$  over the ScS, GSL, BoF, LS, NFS, and GB. In the GoM, the slope water region of the seCS, and deep ocean waters off the LS, NFS, and GB, the simulated March-mean SST in 2018 ranges from  $5^\circ\text{C}$  to  $15^\circ\text{C}$ . Over the deep waters to the south of the seCS, the simulated monthly-mean SST is relatively warm and ranges from  $15^\circ\text{C}$  to  $22^\circ\text{C}$ . Submodel L1 generates some small-scale SST features associated with eddies from, and meanders of, the Gulf Stream in the deep waters to the south of the ScS and GOM. Previous studies demonstrated that, after separating from Cape Hatteras ( $35.5^\circ\text{N}$ ,  $75.5^\circ\text{W}$ ), the Gulf Stream turns eastward and changes from a fast, straight current to a slow, meandering one [34]. These meanders result in warm-core (cold-core) rings pinched off from the northern (southern) side of the Gulf Stream. The warm-core rings (anticyclonic with dimensions of  $\sim 1$  km in the vertical and  $\sim 100$  km in the horizontal directions) entrain warm, salty waters and transport them north to the seCS. Formations of these warm-core rings are associated with Gulf Stream instability processes related to the conversion of potential energy to eddy kinetic energy [35–37]. This physical mechanism also results in many meso-scale and small-scale warm- or cold-core eddies over coastal and slope waters of the ScS. The statistical studies of Brown et al. [38] and Auer [39] indicated that the generation of warm-core rings by the Gulf Stream peaks in the summer months.

The simulated September-mean SST in 2018 (Figure 5c) ranges from  $5^\circ\text{C}$  to  $10^\circ\text{C}$  over the LS and adjacent deep waters, due mainly to the effect of the Labrador Current, which transports relatively cold and fresh waters equatorward from high latitudes. Over the northern GSL, inshore waters off southern Newfoundland, and coastal waters of the eastern NFS, the simulated monthly-mean SST is relatively warm and ranges between  $10^\circ\text{C}$  and  $15^\circ\text{C}$ . Over the southern GSL, ScS, and southwestern NFS, the simulated September-mean SST is between  $15^\circ\text{C}$  and  $21^\circ\text{C}$ . Over the deep waters, the monthly-mean SST is warm and ranges between  $25^\circ\text{C}$  and  $28^\circ\text{C}$ . Submodel L1 also simulates small-scale SST features associated with thermal fronts over the southern GSL, ScS, GoM, and GeB.

The March and September-mean SSTs produced by submodel L1 for 2018 (Figure 5a,c) are compared with their counterparts from the daily GHRSSST Level 4 dataset (Figure 5b,d). Submodel L1 reproduces reasonably well the general features of observed March-mean SST over the L1 domain (Figure 5a,b), including the observed warm SST in the deep ocean waters off the seCS and observed cold SST over the GSL, ScS, LS, NFS and GB. Submodel L1 also has reasonable skills in reproducing the general thermal fronts over

the seCS, including the length scales and general locations. Submodel L1 cannot simulate the exact positions or sizes of observed small-scale SST features, such as the meso-scale eddies and meanders associated with the Gulf Stream and Labrador Current. Due to their nonlinear characteristics, accurate simulations of meso-scale eddies and meanders require data assimilation. Noticeable differences between the simulated and observed March-mean SST also occur over some local areas, including the GoM and swScS. Over these areas, the simulated SST is slightly warmer than the observations. One possible explanation is that the wind-induced mixing and advection over these areas may not be reproduced well by submodel L1 due to the relatively coarse horizontal resolution of model bathymetry over these areas. Another plausible reason is that the March-mean SST over these areas is affected by frontal structures, which submodel L1 cannot accurately generate. It should also be noted that some SST satellite remote sensing data have relatively low accuracy over coastal waters [40].

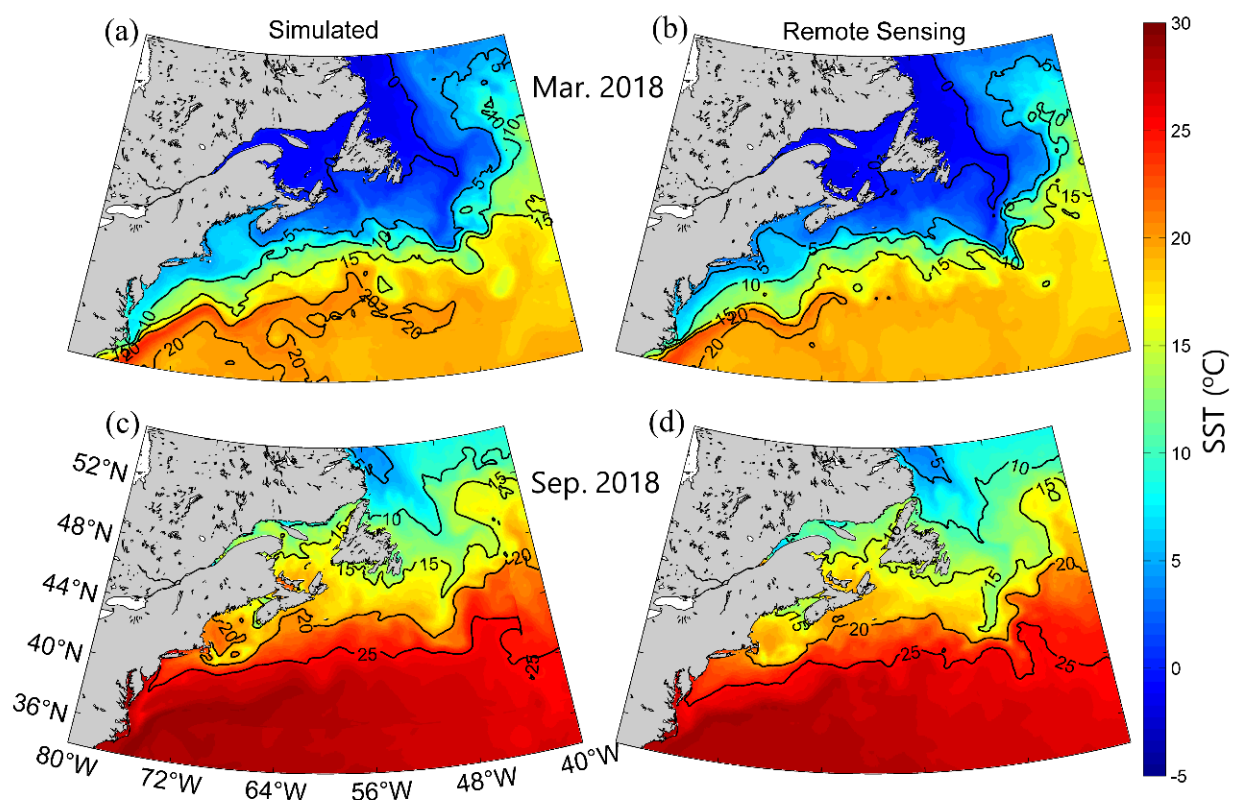


**Figure 5.** Monthly-mean sea surface temperature (SST) over the submodel L1 domain in (a,b) March and (c,d) September 2018 from (a,c) the results of submodel L1 and (b,d) satellite remote sensing SST data.

Submodel L1 has satisfactory skills to reproduce the main features of the observed monthly-mean SST in September 2018 (Figure 5c). Submodel L1 reproduces the observed low SST over the LS and adjacent deep waters, the observed moderately high SST over the ScS and southern NFS, and the observed high SST over deep ocean waters off the seCS. In addition, submodel L1 also reproduces the general distribution of the observed SST over the GSL, including the relatively low SST off northwestern Anticosti Island (AI). Submodel L1 also has reasonable skills in reproducing the observed SST features associated with thermal fronts and the meandering slope water jet over slope waters of the seCS and Newfoundland-Labrador Shelves. The length scales and general locations of simulated and observed thermal fronts generally agree. Noticeable differences occur, however, between the simulated and observed SSTs over several local areas, including the cold water tongue over the GB. The simulated Gulf Stream slightly overshoots northward in this month, pushing back the cold water tongue (resulting from the equatorward Labrador Current) over the GB. Submodel L1 also slightly overestimates the SST over the western GoM and

BoF. One possible explanation is that the overshooting of the simulated Gulf Stream results in the transport of excess warm surface waters to the GoM. Another possible explanation is model error in simulating the horizontal and vertical mixing.

The simulated monthly-mean SSS in March 2018 (Figure 6a) is relatively low and ranges from 25 to 29 (psu) over the SLE and coastal waters off Prince Edward Island (PEI). Over the BoF, GoM, ScS, eastern GSL, LS, NFS, and the GB, the simulated monthly-mean SSS is generally between 30 and 34. The SSS over the inner ScS is relatively low, due mainly to the southwestward alongshore outflow from the southeastern GSL. Over deep waters off the seCS, the SSS is relatively high and ranges from 34 to 37. Submodel L1 also generates some relatively fine-scale salinity frontal structures over slope water regions of the seCS and adjacent deep waters.

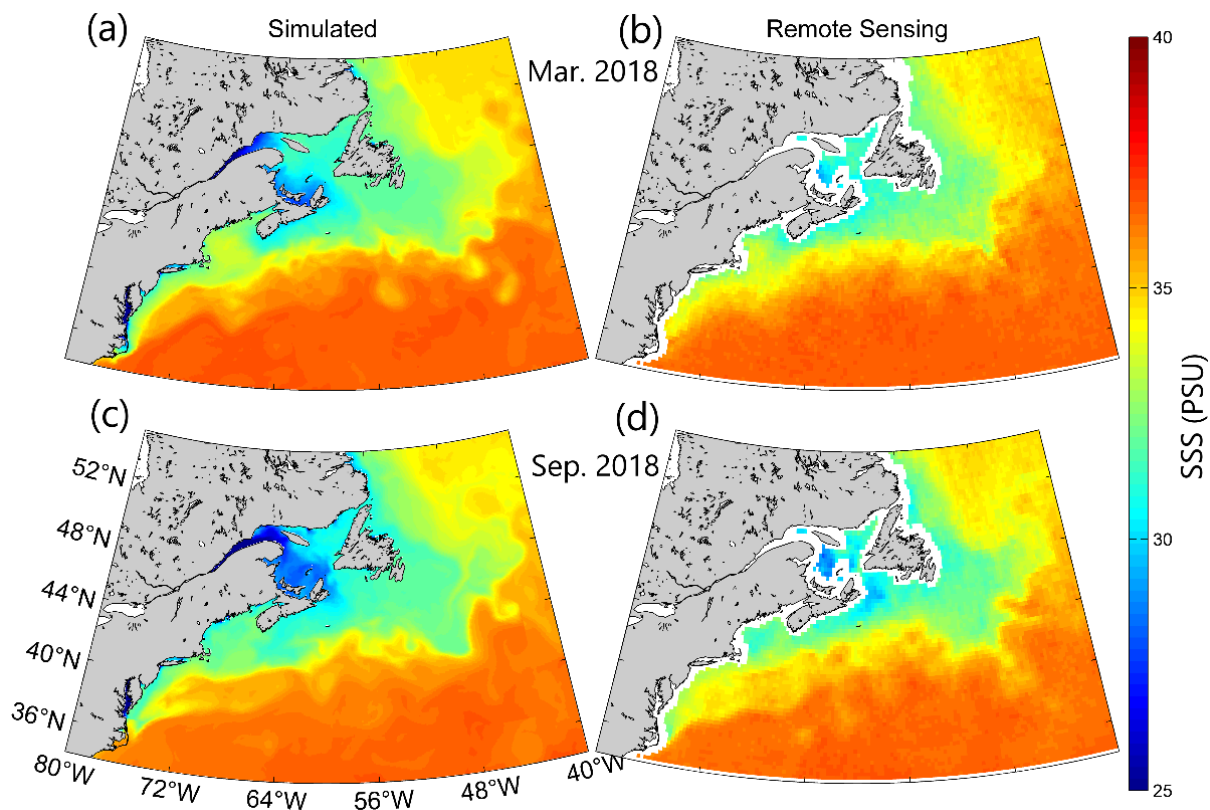


**Figure 6.** The monthly-mean sea surface salinity (SSS) over the L1 domain in (a,b) March and (c,d) September 2018 from (a,c) the results of submodel L1 and (b,d) SSS remote sensing data.

The simulated monthly-mean SSS in September 2018 ranges from 25 to 29 over most of the western GSL and coastal waters off Cape Breton Island (CBI). Over the western GSL and coastal waters off CBI, the monthly-mean SSS is lower in September than in March 2018. Previous studies have demonstrated that the SSS in the GLS, ScS, and GoM is significantly affected by the discharge from major rivers in the region, including the SLR. The monthly-mean SLR discharge data constructed by the SLGO for the period December 2017–December 2018 were largest during March–June 2018 ( $1.3\text{--}1.8 \times 10^4 \text{ m}^3 \text{ s}^{-1}$ ). Ohashi and Sheng [41] demonstrated that the freshwater signal from the SLE takes about 100 days to reach Cabot Strait. Therefore, the relatively low SSS over the western GSL and off CBI in the summer (relative to the winter) in 2018 is due mainly to the seaward transport of the large SLR discharge during the spring season (particularly between March and June). In addition, the stronger vertical stratification in the summer than in the winter also partially contributes to the seasonal SSS differences between winter and summer.

A comparison between the simulated SSS (Figure 6a,c) and the satellite remote sensing data (Figure 6b,d) demonstrates that submodel L1 reproduces reasonably well the general

large-scale features of monthly-mean SSS in March and September 2018 over the model domain. The model reasonably reproduces the observed high SSS over deep waters off the seCS and the observed low SSS over coastal and shelf waters of the seCS in these two months. Over the GSL, the simulated SSS (Figure 6a,c) is also comparable with the remote sensing data (Figure 6b,d), although the remote sensing SSS is unavailable near the coast of the GSL. Submodel L1 also has satisfactory skills in reproducing the observed features associated with salinity fronts over the slope waters of the L1 domain, including the typical length scales and general locations of the monthly-mean salinity fronts. It should be noted that the simulated temperature and salinity are prognostic in the top 30 m of the water column, although the semi-prognostic method is applied everywhere.

To assess the model performance in reproducing the temporal variability of temperature, the daily-mean simulated SSTs (produced by submodel L2) averaged over the green boxes (Figure 1b) in the swScS (Figure 7a; blue line) and central GoM (Figure 7b, blue line) are respectively compared with their counterparts (Figure 7a,b; red lines) calculated from the daily GHRSSST Level 4 CMC0.1deg Global Foundation Sea Surface Temperature Analysis (GDS version 2).

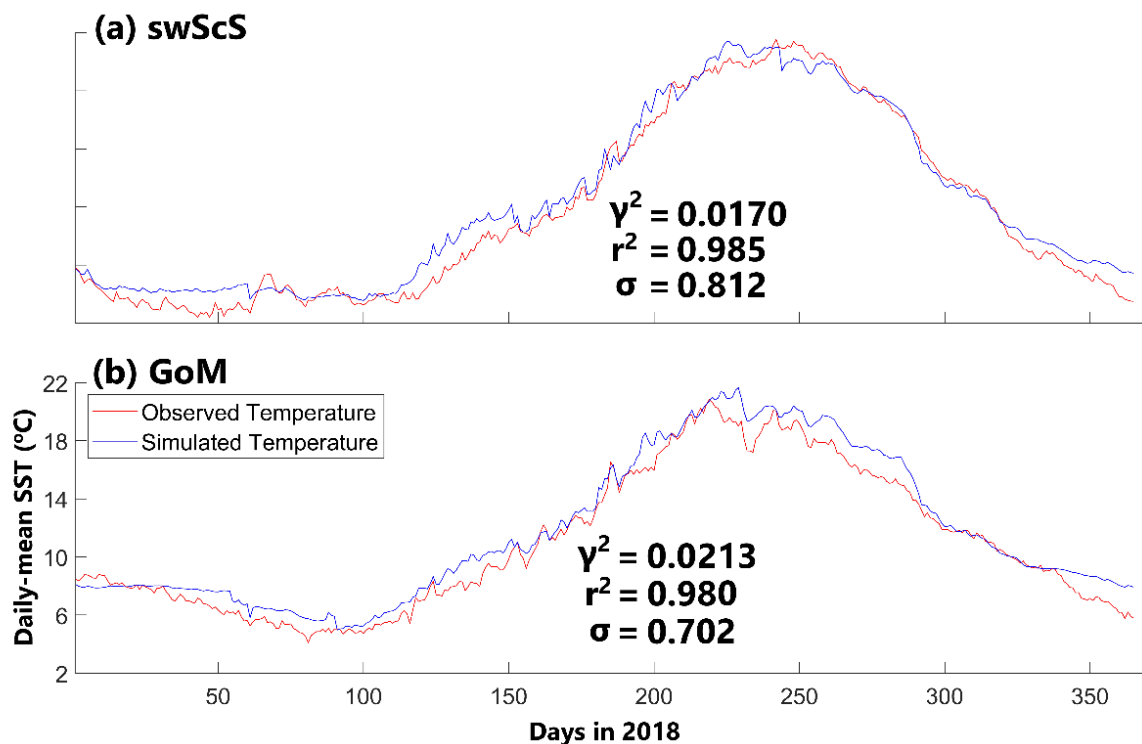


**Figure 7.** Time series of daily-mean SSTs produced by submodel L2 in 2018 (blue lines) averaged over green boxes (a) A (swScS) and (b) B (central GoM) in Figure 1b. The red lines represent the time series of remote sensing SST observations extracted from the daily GHRSSST Level 4 CMC0.1deg Global Foundation Sea Surface Temperature Analysis (GDS version 2).

In the swScS (green box A; Figure 1b), the daily observed SST gradually decreased from  $\sim 5.6$  °C to  $\sim 2.7$  °C between 1 January and 2 February 2018, mainly due to the negative surface heat fluxes in winter. From 4 February to 16 April in 2018, the daily observed SST in the swScS remained nearly constant ( $\sim 3.8$  °C) with several large oscillations. From 17 April to 6 September 2018, the daily observed SST in the swScS gradually increased from  $\sim 3.8$  °C to  $\sim 21$  °C mainly due to the positive net heat flux at the sea surface from early spring to late summer. From 6 September to 31 December 2018, the daily observed SST in the swScS decreased from  $\sim 21$  °C to  $\sim 3.5$  °C mainly due to the negative surface heat fluxes. The daily observed SST in the central GoM (Figure 7b) shows a temporal variability highly comparable to the counterpart in the swScS, except for the relatively

higher values in the central GoM than in the swScS. A comparison between model results and remote sensing observations indicates that the NGMS-seCS has satisfactory skills in reproducing the seasonal cycle of SST in the swScS (central GoM), with the correlation square of  $\sim 0.985$  ( $\sim 0.980$ ),  $\gamma^2$  of  $\sim 0.017$  ( $\sim 0.0213$ ), and standard deviation of  $\sim 0.812$  °C ( $\sim 0.702$  °C). The NGMS-seCS also has noticeable deficiencies in reproducing the observed SST oscillations on the  $O$  (days) time scale. One plausible reason is the accuracy of the atmospheric forcing used in the NGMS-seCS. Another plausible reason is model errors in simulating the sub-grid mixing and fine-scale nonlinear circulation features. The seasonal variability of the vertical stratification in the swScS (green box A in Figure 1b) is discussed in Appendix G.

#### 4. Process Study: Effects of Winds and Tides on Hydrography and Circulation

For convenience, a new coordinate system (Figure 1c) is used in this section to examine the temporal and spatial variability of model results over the swScS. The x-axis of this new coordinate system is aligned with the Atlantic coast of Nova Scotia and is positive to the northeast; the y-axis is in the cross-shelf direction and positive to the northwest. Two of the three transects used in this section are defined on this coordinate system. Transect PP' originates from Liverpool Bay, Nova Scotia, and is parallel to the y-axis. Transect PQ (Figure 1b) is the extension of Transect PP' over the L2 domain. The third transect, EE', is a north-south transect originating from Yarmouth, Nova Scotia.

##### 4.1. Effects of Winds

To examine the role of wind forcing over the GSL-ScS-GoM region and adjacent deep waters, the monthly-mean model results produced by submodel L2 in case CR are compared to their counterparts in case NW. Model results in February and August 2018 are chosen to represent the typical winter and summer months.

The February-mean SST ( $\bar{T}_0^{CR}$ ; Figure 8a) in 2018 has the typical horizontal distribution in the winter months, which is relatively cool and varies between  $-2$  °C and  $5$  °C over the ScS, GSL, BoF, and southwestern NFS. Over the GoM and slope water region off the ScS,  $\bar{T}_0^{CR}$  varies between  $5$  °C and  $15$  °C. In the deep ocean waters to the south of the slope waters,  $\bar{T}_0^{CR}$  is warm and ranges between  $15$  °C and  $21$  °C. The February-mean surface circulation ( $\vec{U}_0^{CR}$ ) also has many recognized features over the region, including the seaward surface currents over the southeastern GSL, spatially-varying currents on the ScS and GoM, the northeastward jet over the slope water region off the ScS, and the northern part of the Gulf Stream and associated eddies and meanders in the deep waters to the south of the slope water region (Figure 8a). Both  $\bar{T}_0^{CR}$  and  $\vec{U}_0^{CR}$  in this month also have small-scale features associated with the warm- and cold-core rings, thermal fronts, and the meandering of the slope water jet over the slope waters and adjacent deep ocean waters off the ScS-GoM.

The February-mean sub-surface (40 m) temperature and currents ( $\bar{T}_{40}^{CR}$  and  $\vec{U}_{40}^{CR}$ ; Figure 8d) in 2018 have large-scale horizontal features highly similar to their counterparts at the sea surface in case CR (Figure 8a), except for the weaker current magnitudes at 40 m. The weak vertical stratification in the top 40 m over the L2 domain in winter months results from both the winter convection and intense wind-induced vertical mixing. Winter convection is referred to as the sinking process of cold surface waters to deeper depths due to the largely negative net heat flux at the sea surface (i.e., the ocean water losses heat to the air) in the late fall and winter months, which is one of the important processes over the ECS. The Nova Scotia Current [42], which is a southwestward coastal jet over the inner shelf of the ScS, is approximately compensated by the northeastward wind-driven currents in the surface mixed layer in February 2018.

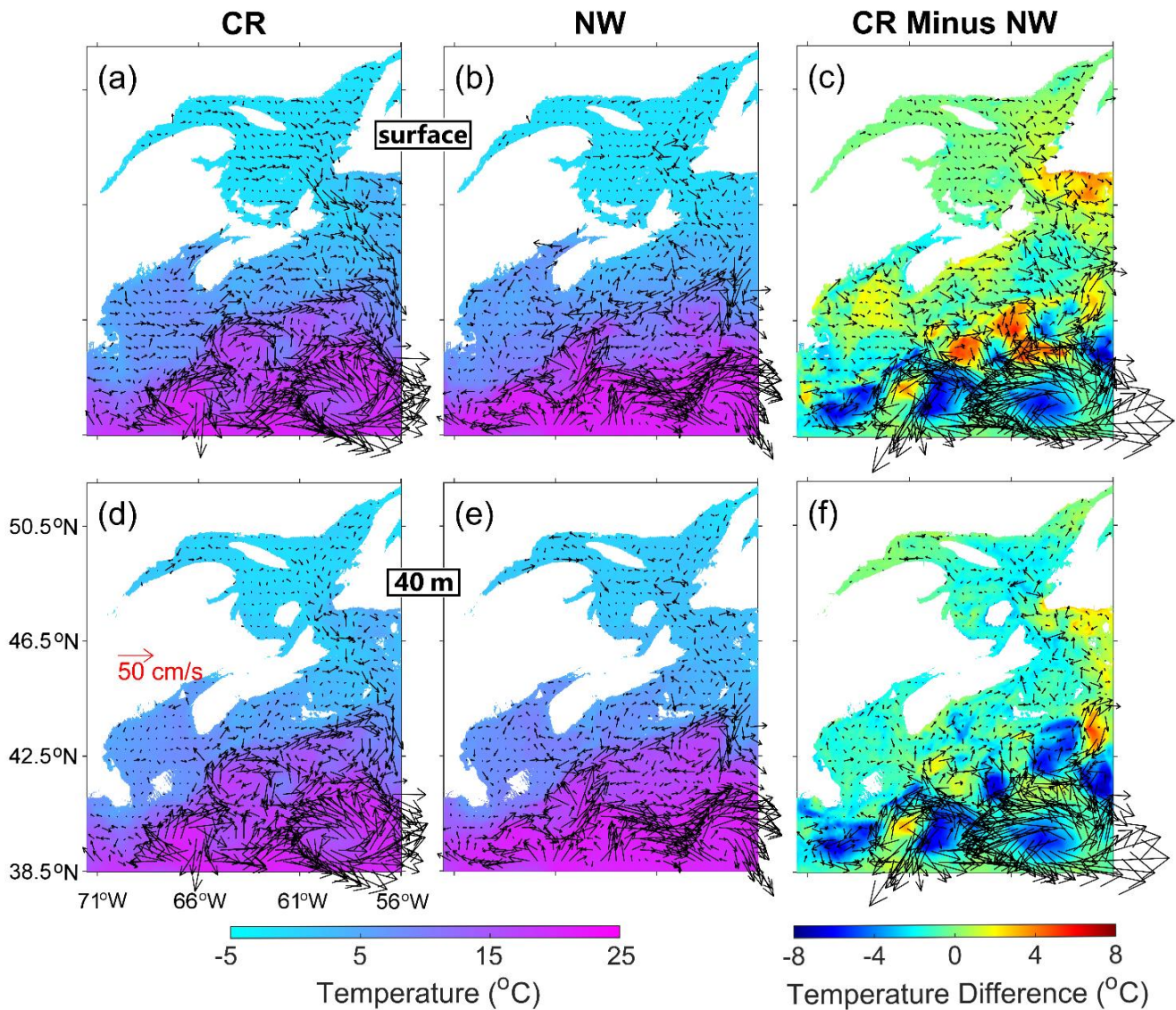


**Figure 8.** Monthly-mean currents and temperature in February 2018 produced by submodel L2 at (a,b) the sea surface and (d,e) 40 m over the L2 domain in cases (a,d) CR and (b,e) NW. Differences in the monthly-mean currents and temperature between cases CR and NW at (c) the sea surface and (f) 40 m. For clarity, velocity vectors are plotted at every 14th model grid point.

The February-mean SST ( $\bar{T}_0^{NW}$ ; Figure 8b) in 2018 in case NW is very similar to, and slightly cooler than, the counterpart in case CR over the coastal and shelf waters, including the GSL, ScS, and GoM. In the slope waters and adjacent deep ocean waters off the ScS-GOM, the February-mean SST in case NW, particularly the small-scale SST features associated with eddies and meanders, significantly differs from the counterpart in case CR.

The February-mean surface currents in case NW ( $\bar{U}_0^{\rightarrow NW}$ ; Figure 8b) also significantly differ from the counterparts in case CR, particularly in the slope and adjacent deep ocean water regions. This indicates the importance of the wind forcing in surface currents and SST in the winter months over the L2 domain in case CR.

The monthly-mean sub-surface (40 m) temperature and currents in case NW ( $\bar{T}_{40}^{NW}$ ,  $\bar{U}_{40}^{\rightarrow NW}$ ; Figure 8e) are highly similar to the counterparts at the sea surface ( $\bar{T}_0^{NW}$  and  $\bar{U}_0^{\rightarrow NW}$ ; Figure 8b) in February 2018, indicating that the vertical stratification of hydrography in this month is very weak in the top 40 m in case NW due to the winter convection mentioned

above. The February-mean fields of  $(\overline{T}_{40}^{NW}, \overrightarrow{U}_{40}^{NW})$  in 2018 in case NW differ from the counterparts in case CR over the slope waters and beyond, indicating the important role of wind forcing on the sub-surface currents. It should be noted that the large February-mean currents in case NW (Figure 8b,e) are driven by the baroclinic dynamics, nonlinear tidal processes, and boundary forcing, since wind forcing is excluded in this case.

The differences in the monthly-mean model results between cases CR and NW are used to quantify the accumulative effect of wind forcing on the 3D circulation and hydrography. Over much of the coastal and shelf waters in the L2 domain, the differences in the February-mean SST between cases CR and NW ( $\Delta\overline{T}_0^{CR-NW}$ ; Figure 8c) are positive and up to 3 °C. The differences in the February-mean sub-surface (40 m) temperature between the two cases ( $\Delta\overline{T}_{40}^{CR-NW}$ ; Figure 8f) are mostly negative and up to −2 °C over the coastal and shelf region. Over the seCS, the vertical stratification in the surface mixed layer is weak in winter mainly due to strong winter convection. The wind-induced vertical mixing further blends the relatively warm subsurface waters with the relatively cool surface waters in the surface mixed layer. This explains why the wind forcing makes the SST warmer and sub-surface temperature cooler, as shown in Figure 8c,f. The monthly-mean current differences between these two cases at the sea surface ( $\Delta\overrightarrow{U}_0^{\rightarrow CR-NW}$ ; Figure 8c) and 40 m ( $\Delta\overrightarrow{U}_{40}^{\rightarrow CR-NW}$ ; Figure 8f) over the coastal and shelf waters represent the currents directly and indirectly driven by winds in the winter months.

Over several coastal areas of the L2 domain, such as the BoF, GeB, and the inner shelf off Yarmouth, the tidal forcing is very strong, resulting in particularly weak vertical stratification of hydrography in February 2018. As a result, sensible and latent heat fluxes play important roles in affecting the February-mean SST than the wind-induced vertical mixing over these areas, with negative  $\Delta\overline{T}_0^{CR-NW}$  of about −2 °C in February 2018 (Figure 8c).

Over the slope waters and deep ocean waters off the ScS-GoM, there are significantly large differences in the February-mean temperature and currents between cases CR and NW (Figure 8c,f). In addition to the effect of wind-induced mixing and currents mentioned above, these large differences are generated by the wind-induced modulation of large-scale circulation (i.e., the Gulf Stream), warm/cold-core rings, and thermal fronts in case CR. The effect of wind forcing on currents can be categorized into direct and indirect types. The direct effects of wind forcing include the wind-driven currents and shelf waves excited by winds. The indirect effects include density-driven currents that are ultimately driven by winds, as well as wind-induced modulations of nonlinear circulation features, such as eddies, rings, and frontal structures. In the winter months, the wind forcing over the seCS is typically strong, and thus significantly modifies the nonlinear features of the hydrography and circulation over the slope water region and adjacent deep waters. The modulation of hydrography, in return, modifies density-driven currents and baroclinic hydrodynamics. As a result, the simulated Gulf Stream in case NW shows significantly different circulation features and eddies/meanders from their counterparts in case CR. These large current differences are associated mainly with wind-induced modulations of large-scale circulation, rather than the wind-driven currents. In addition, the wind forcing modifies the locations and intensities of warm-core rings pinched off from the northern side of the Gulf Stream. As mentioned earlier, the warm-core rings are clockwise and measured about 1 km vertically [34]. As a result, the differences between cases CR and NW in terms of monthly-mean temperatures in February 2018 are positive (negative) over clockwise (counterclockwise) circulation differences, as shown in Figure 8c,f.

In contrast to the weak vertical stratification in the surface mixed layer in winter, strong thermal stratification occurs at the bottom of the thin surface mixed layer in summer over the seCS, mostly due to the large surface heating and relatively weak wind-induced vertical mixing in late spring and summer [43]. The thickness of the surface mixed layer (about 10 m) in the summer months is also much thinner than its counterpart (about 50 m) in the winter months [44].

The monthly-mean SST ( $\bar{T}_0^{CR}$ ; Figure 9a) in August 2018 in case CR also has typical horizontal distribution in summer months, which is moderately warm and ranges between 10 °C and 20 °C over the northern GSL, BoF, and southwestern NFS, and between 14 °C and 21 °C over the central ScS. Over the central and western GoM, the slope water region off the ScS, and coastal waters off PEI,  $\bar{T}_0^{CR}$  is warmer and ranges between 20 °C and 25 °C in this month in case CR. Over deep waters off the ScS-GoM,  $\bar{T}_0^{CR}$  is warmest and ranges between 25 °C and 27 °C in this month (Figure 9a). It should be noted that  $\bar{T}_0^{CR}$  is relatively cool over the BoF, GeB, and coastal waters off Yarmouth in this month, mainly due to strong tidal mixing and tidal rectification. The relatively cool monthly-mean SST over the inner ScS in August 2018 in case CR (Figure 9a) indicates coastal upwelling driven by winds in summer.

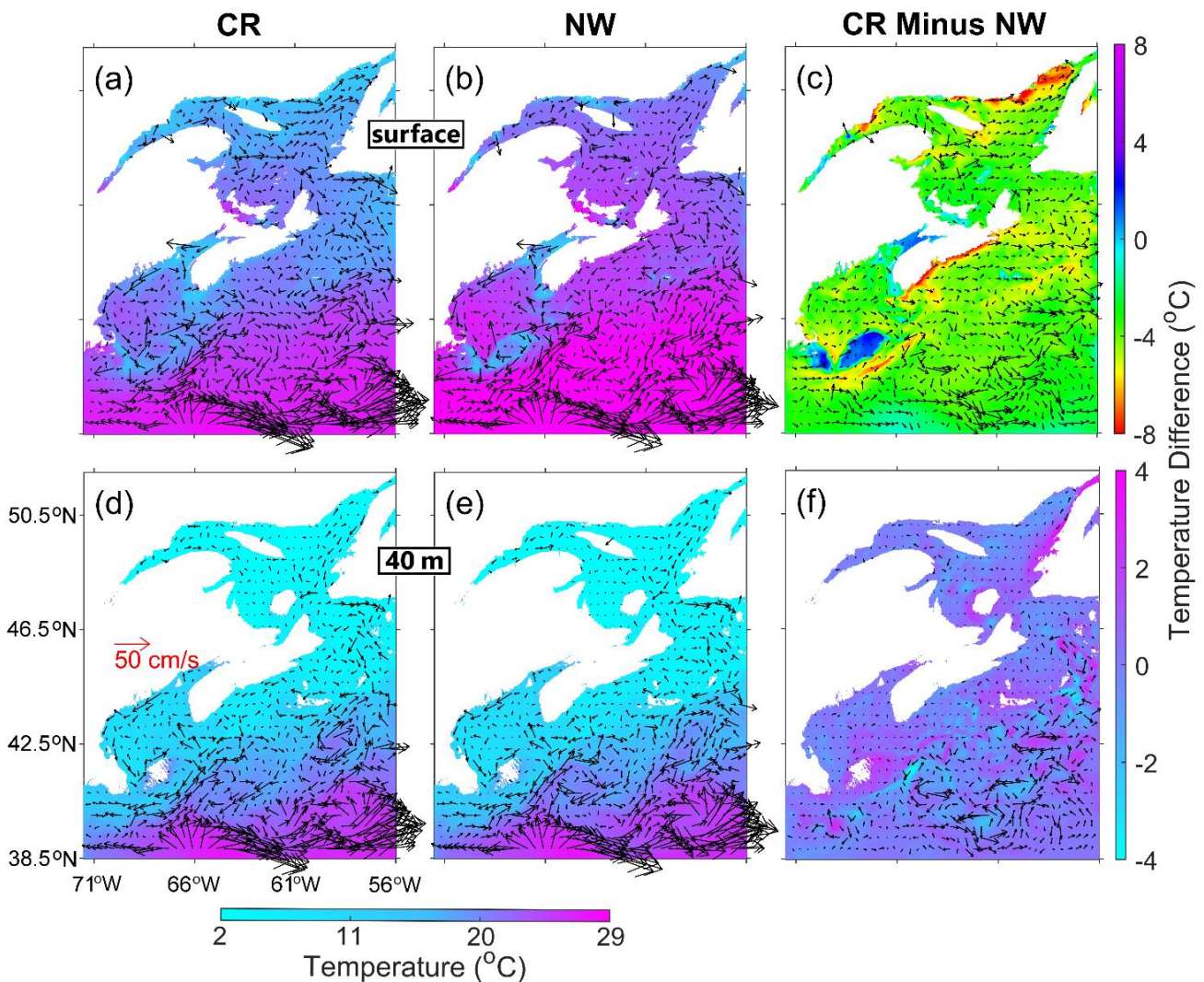


**Figure 9.** Monthly-mean currents and temperature in August 2018 produced by submodel L2 at (a,b) the sea surface and (d,e) 40 m over the L2 domain in cases (a,d) CR and (b,e) NW. Differences in the monthly-mean currents and temperature between cases CR and NW at (c) the sea surface and (f) 40 m. For clarity, velocity vectors are plotted at every 14th model grid point.

The August-mean surface currents ( $\vec{U}_0^{\rightarrow CR}$ ; Figure 9a) in 2018 in case CR have many well-known large-scale surface circulation features, including the southeastward outflow associated with the seaward spreading of the freshwater discharge from the SLR over the southeastern GSL, the relatively intense southwestward flow along the coast of the western GoM, and the strong flow, eddies, and meanders associated with the Gulf Stream



in the slope waters and adjacent deep ocean waters. In this month,  $\bar{U}_0^{\rightarrow CR}$  is southeastward (seaward) over the southwestern GSL, and northeastward over the eastern GSL, except for coastal waters off western Newfoundland. Both  $\bar{U}_0^{\rightarrow CR}$  and  $\bar{T}_0^{CR}$  in August 2018 also show fine-scale features of circulation and SST associated with the local tidal mixing/advection and topographic steering over GeB (e.g., the anticyclonic circulation along isobaths around GeB) and adjacent (Figure 9a).

Due to strong thermal stratification at the bottom of the thin surface mixed layer resulting from the positive surface heat fluxes in summer, the August-mean sub-surface (40 m) temperature ( $\bar{T}_{40}^{CR}$ ) significantly differs from the August-mean SST ( $\bar{T}_0^{CR}$ ). In this month,  $\bar{T}_{40}^{CR}$  in case CR (Figure 9d) is relatively cool, ranging between 2 °C and 4 °C over the GSL, northeastern ScS, and southwestern NFS. Over the eastern GoM and swScS,  $\bar{T}_{40}^{CR}$  is about 10 °C. Over the BoF, southern GoM, and slope waters off the ScS-GoM,  $\bar{T}_{40}^{CR}$  ranges between 10 °C and 20 °C. In deep ocean waters to the south of the slope waters,  $\bar{T}_{40}^{CR}$  is significantly warmer and ranges between 20 °C and 26 °C.

In the GoM and over the slope waters and adjacent deep ocean waters off the ScS-GoM, the monthly-mean sub-surface (40 m) currents ( $\bar{U}_{40}^{\rightarrow CR}$ ; Figure 9d) have large-scale circulation features similar to their counterparts at the sea surface ( $\bar{U}_0^{\rightarrow CR}$ ; Figure 9a) in August 2018 in case CR. Over these regions, the August-mean sub-surface circulation in case CR (Figure 9d) features the large-scale cyclonic coastal currents in the GoM, the slope water jet, the northern part of the Gulf Stream, and associated eddies and meanders at 40 m. In the GSL and ScS, by comparison, the August-mean sub-surface (40 m) currents significantly differ from their counterparts at the sea surface, mainly due to the strong vertical stratification of hydrography at the bottom of the thin surface mixed layer in the summer months. In the GSL, the August-mean sub-surface currents in case CR are very weak over the southwestern region, and have an anticyclonic recirculation over the eastern region with a narrow southwestward jet along the coast of eastern Newfoundland (Figure 9d). Over the inner ScS, the Nova Scotia Current is much more well-defined at 40 m than at the sea surface (Figure 9a,d) in the summer months.

Without wind forcing in case NW, the simulated August-mean SST ( $\bar{T}_0^{NW}$ ; Figure 9b) in 2018 is relatively warm and about 24 °C in the GSL, except for several coastal waters over the northern GSL. Over the ScS and GoM,  $\bar{T}_0^{NW}$  in this month varies between 24 °C and 27 °C, except for relatively low SST over coastal and shallow areas with strong tidal mixing/advection in the GoM, including the GeB and BoF. In the slope waters and deep ocean waters,  $\bar{T}_0^{NW}$  in this month is warm and varies between 27 °C and 29 °C (Figure 9b). Without wind-inducing vertical mixing,  $\bar{T}_0^{NW}$  is warmer than  $\bar{T}_0^{CR}$  in August 2018 over the whole L2 domain, except for areas affected significantly by tidal mixing/advection in the GoM. In case NW, the thermal energy gained from the positive net heat flux at the sea surface (shortwave and longwave radiations) is trapped in the unrealistically thin surface mixed layer in summer due to the absence of wind-induced vertical mixing.

The August-mean surface currents ( $\bar{U}_0^{\rightarrow NW}$ ; Figure 9b) in case NW have large-scale features similar to their counterparts in case CR ( $\bar{U}_0^{\rightarrow CR}$ ; Figure 9a), particularly in the deep ocean waters off the ScS-GoM. Noticeable differences, however, occur between  $\bar{U}_0^{\rightarrow CR}$  and  $\bar{U}_0^{\rightarrow NW}$  over coastal and shelf waters in August 2018. Without wind forcing,  $\bar{U}_0^{\rightarrow NW}$  is seaward as part of the estuarine plume over the southwestern GSL, but is approximately southwestward over the eastern GSL in case NW. The simulated Nova Scotia Current over the inner shelf of the ScS in case NW is unrealistically too strong at the sea surface (Figure 9b) due to the lack of wind forcing in this case.

The large-scale features of the August-mean  $\bar{T}_{40}^{NW}$  and  $\bar{U}_{40}^{\rightarrow NW}$  in case NW (Figure 9e) are highly comparable to their counterparts in case CR (Figure 9d). This indicates that, in summer months, wind forcing is usually weak and does not significantly affect the sub-surface (15 m or deeper) circulation and hydrography, except for coastal waters during upwelling- and/or downwelling-favorable wind events.

Figure 9c presents differences in the monthly-mean SST ( $\Delta\bar{T}_0^{CR-NW}$ ) and surface currents ( $\Delta\bar{U}_0^{\rightarrow CR-NW}$ ) between cases CR and NW in August 2018. The values of  $\Delta\bar{T}_0^{CR-NW}$  are negative over the L2 domain with the maximum negative value of about  $-7^\circ\text{C}$ , except for some local areas affected by strong tidal mixing/advection. This indicates the important role of wind-induced vertical mixing for transferring thermal energy from the sea surface downward. Without wind-induced vertical mixing (case NW), the thermal energy gained from positive surface heat fluxes (shortwave and longwave radiations) is trapped in the very thin surface mixed layer, resulting in unrealistically too warm SSTs in case NW. Positive values of  $\Delta\bar{T}_0^{CR-NW}$  occur over several local areas, including the BoF and GeB (Figure 8c). Over these areas, wind-induced horizontal mixing and advection, as well as the positive net heat flux associated with wind stress (latent and sensible heat fluxes), in case CR significantly counteract the SST cooling generated by the strong tides.

The magnitudes of  $\Delta\bar{U}_0^{\rightarrow CR-NW}$  in August 2018 (Figure 9c) are relatively small at about  $0.1\text{ m s}^{-1}$  over the ScS and GoM, and up to  $0.2\text{ m s}^{-1}$  in the western GSL. Large magnitudes of  $\Delta\bar{U}_0^{\rightarrow CR-NW}$  also occur over the slope waters off the ScS-GoM. The relatively small magnitudes of  $\Delta\bar{U}_0^{\rightarrow CR-NW}$  over the coastal and shelf waters in this month demonstrate the direct effect of wind forcing on the summertime surface circulation. In contrast, the relatively large magnitudes of  $\Delta\bar{U}_0^{\rightarrow CR-NW}$  over the slope waters and in the western GSL are mainly associated with the wind-induced modulations of meanders and eddies. The magnitudes of  $\Delta\bar{U}_0^{\rightarrow CR-NW}$  over the slope waters and adjacent deep ocean waters in August 2018 (Figure 9c) are significantly smaller than their counterparts in February 2018 (Figure 8c), indicating that the wind forcing and wind-induced modulations of large-scale circulation are generally much weaker and smaller in the summer than in the winter.

Figure 9f demonstrates that, in August 2018,  $\Delta\bar{T}_{40}^{CR-NW}$  is positive over the L2 domain, except for several patches with negative values over the slope waters off the ScS-GoM. The positive values of  $\Delta\bar{T}_{40}^{CR-NW}$  indicate that subsurface waters are cooler in case NW than in case CR in this month. This can be explained by the fact that the incoming heat fluxes at the sea surface could not easily penetrate downward without wind-induced vertical mixing (case NW) in the summer months. There are many small-scale features with noticeable negative values of  $\Delta\bar{T}_{40}^{CR-NW}$  over the slope waters and deep ocean waters off the ScS-GoM (Figure 9f), indicating the modulation effect of wind forcing on mesoscale eddies and recirculation over these regions. There are also several small-size patches and narrow strips of negative values of  $\Delta\bar{T}_{40}^{CR-NW}$  ( $\sim -1^\circ\text{C}$ ) over coastal and shelf waters (Figure 9f), such as the western ScS, associated with wind-induced modulation of small-scale nonlinear dynamics.

The magnitudes of  $\Delta\bar{U}_{40}^{\rightarrow CR-NW}$  in August 2018 (Figure 9f) are relatively small over coastal and shelf waters in the L2 domain, due to the fact that winds are generally weak in August and the direct effect of wind forcing on the 3D circulation mainly occurs in the top 10 m. Over slope waters and deep ocean waters off the ScS-GOM, by comparison, the values of  $\Delta\bar{U}_{40}^{\rightarrow CR-NW}$  in this month are relatively large, which are mainly associated with the wind-induced modulation in the locations and intensities of meanders and warm/cold-core eddies.

The accumulative effect of winds on the monthly-mean salinity fields in the two months is examined next based on model results in cases CR and NW. In February 2018, the monthly-mean SSS ( $\bar{S}_0^{CR}$ ; Figure 10a) in case CR is relatively low and ranges between 27 and 32 (psu) over the SLE, southern GSL, and inner shelf of the ScS (Figure 10a). Over the GoM,  $\bar{S}_0^{CR}$  is typically about 33. Over the slope waters off the ScS-GoM,  $\bar{S}_0^{CR}$  ranges between 32 and 35. In the deep ocean waters to the south of the slope waters,  $\bar{S}_0^{CR}$  is high and generally above 35. In this month,  $\bar{S}_0^{CR}$  also has some fine-scale features associated with salinity fronts and nonlinear circulation.

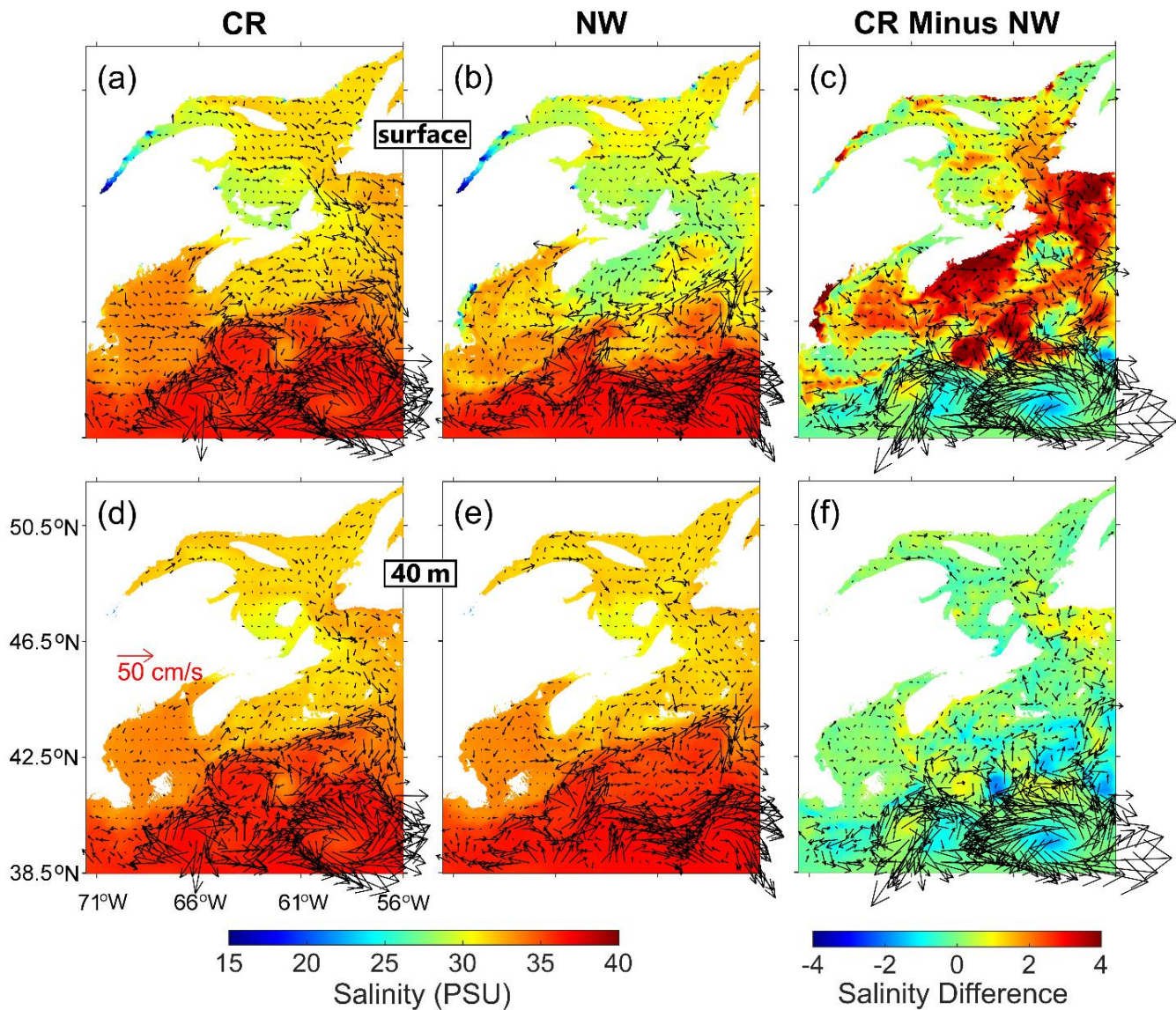


**Figure 10.** Monthly-mean currents and salinity in February 2018 produced by submodel L2 at (a,b) the sea surface and (d,e) the 40-m depth over the L2 domain in cases (a,d) CR and (b,e) NW. Differences in salinity and currents between cases CR and NW at (c) sea surface and (f) 40 m. For clarity, velocity vectors are plotted at every 14th model grid point. The current velocity vectors are identical to those shown in Figure 8.

The February-mean sub-surface (40 m) salinity ( $\bar{S}_{40}^{CR}$ ; Figure 10d) in 2018 has a horizontal distribution very similar to  $\bar{S}_0^{CR}$  (Figure 10a), except for the relatively higher values at 40 m over the SLE, southern GSL, and the inner shelf of the ScS. The high similarity between  $\bar{S}_0^{CR}$  and  $\bar{S}_{40}^{CR}$  in this month is mainly due to winter convection and the strong

wind-induced vertical mixing in winter. It should be noted that a sharp salinity front approximately follows along the shelf break of the ScS-GoM (Figure 10a,d), which forms an important frontal boundary separating the relatively cool and fresh shelf waters from the warm and salty slope and deep ocean waters [45].

Without wind forcing in case NW, the February-mean SSS ( $\bar{S}_0$ ; Figure 10b) in 2018 is lower than the counterpart in case CR (Figure 10a) over the eastern GSL, southwestern NFS, ScS, eastern GoM, and coastal waters near river mouths in the northern GSL and western GoM. This indicates the important effect of wind-induced mixing on the salinity distribution in the surface mixed layer and seaward spreading of low-salinity waters over the southwestern GSL and eastern and inner ScS in the winter months. These low-salinity waters are associated with the seaward (equatorward) spreading of estuarine waters from the SLE [41]. Without wind-induced vertical mixing (case NW), the low-salinity waters are unrealistically trapped within the very thin surface layer. Strong winds in this month also modify the salinity distributions over the slope waters and adjacent deep waters through wind-induced modulations of baroclinic dynamics and nonlinear circulation features in the upper water columns.

Over the coastal and shelf waters of the L2 domain, the monthly-mean sub-surface (40 m) salinity ( $\bar{S}_{40}^{NW}$ ; Figure 10e) in February 2018 in case NW has large-scale features highly similar to the counterpart in case CR ( $\bar{S}_{40}^{CR}$ ; Figure 10d), due to the winter convection. Significantly large differences between  $\bar{S}_{40}^{NW}$  and  $\bar{S}_{40}^{CR}$  occur over the slope waters and deep ocean waters off the ScS-GoM, mainly due to the large modulation effect of wind forcing on mesoscale eddies and warm/cold-core rings over these regions. A sharp salinity front also occurs at the shelf break of the ScS-GoM in this month in case NW.

Figure 10c presents the differences in February-mean SSS in 2018 between cases CR and NW ( $\Delta\bar{S}_0^{CR-NW}$ ). The salinity differences are significantly positive over the southwestern NFS, inner and middle ScS, and coastal waters of the GoM, with the maximum positive value of about 4. Due to the important effect of wind forcing on large-scale circulation and associated eddies and meanders over the slope waters and adjacent deep ocean waters off the ScS-GoM, large negative (positive) values of  $\Delta\bar{S}_0^{CR-NW}$  are associated with cyclonic (anticyclonic) rings of  $\Delta\bar{U}_0$  (Figure 10c) in February 2018.

At 40 m, due to winter convection, the monthly-mean sub-surface salinity differences between cases CR and NW ( $\Delta\bar{S}_{40}^{CR-NW}$ ; Figure 10f) in February 2018 are relatively small in the GSL, ScS, and GoM, except for some coastal areas due to the local wind effects. In the slope waters and adjacent deep ocean waters,  $\Delta\bar{S}_{40}^{CR-NW}$  is relatively large, with large negative (positive) values associated with the cyclonic (anti-cyclonic) currents of  $\Delta\bar{U}_{40}$ , mainly due to the modulation effect of wind forcing as mentioned above.

In August 2018, the monthly-mean SSS ( $\bar{S}_0^{CR}$ ; Figure 11a) is relatively low and ranges between 26 and 29 over the western GSL and coastal waters off CBI. The relatively low  $\bar{S}_0^{CR}$  over these areas is due mainly to the large discharge from the SLR during the spring and subsequent propagation of the low-salinity estuarine plume. Over the eastern GSL, southwestern NFS, GoM, and coastal waters of the ScS (except for coastal waters off CBI),  $\bar{S}_0^{CR}$  generally ranges from 30 to 32. Over the slope water region of the ScS,  $\bar{S}_0^{CR}$  ranges from 31 to 34. Over the deep ocean waters off the ScS-GoM,  $\bar{S}_0^{CR}$  is generally above 35. There are some fine-scale SSS features of  $\bar{S}_0^{CR}$  associated with salinity fronts and nonlinear circulation over the GSL, GoM, slope waters of the ScS-GoM, and adjacent deep ocean waters. A salinity front occurs at the shelf break of the ScS-GoM.

Since wind-induced vertical mixing is generally weak in summer, the August-mean sub-surface (40 m) salinity ( $\bar{S}_{40}^{CR}$ ; Figure 11d) in case CR differs from the counterpart at the sea surface (Figure 11a). Over the GSL, ScS and GoM,  $\bar{S}_{40}^{CR}$  in this month is nearly uniform and varies between 32 and 33, with a well-defined salinity front at the shelf break of the

ScS and GoM. In the slope waters and adjacent deep ocean waters off the ScS-GoM,  $\bar{S}_{40}^{CR}$  in this month is high and varies between 35 and 37.

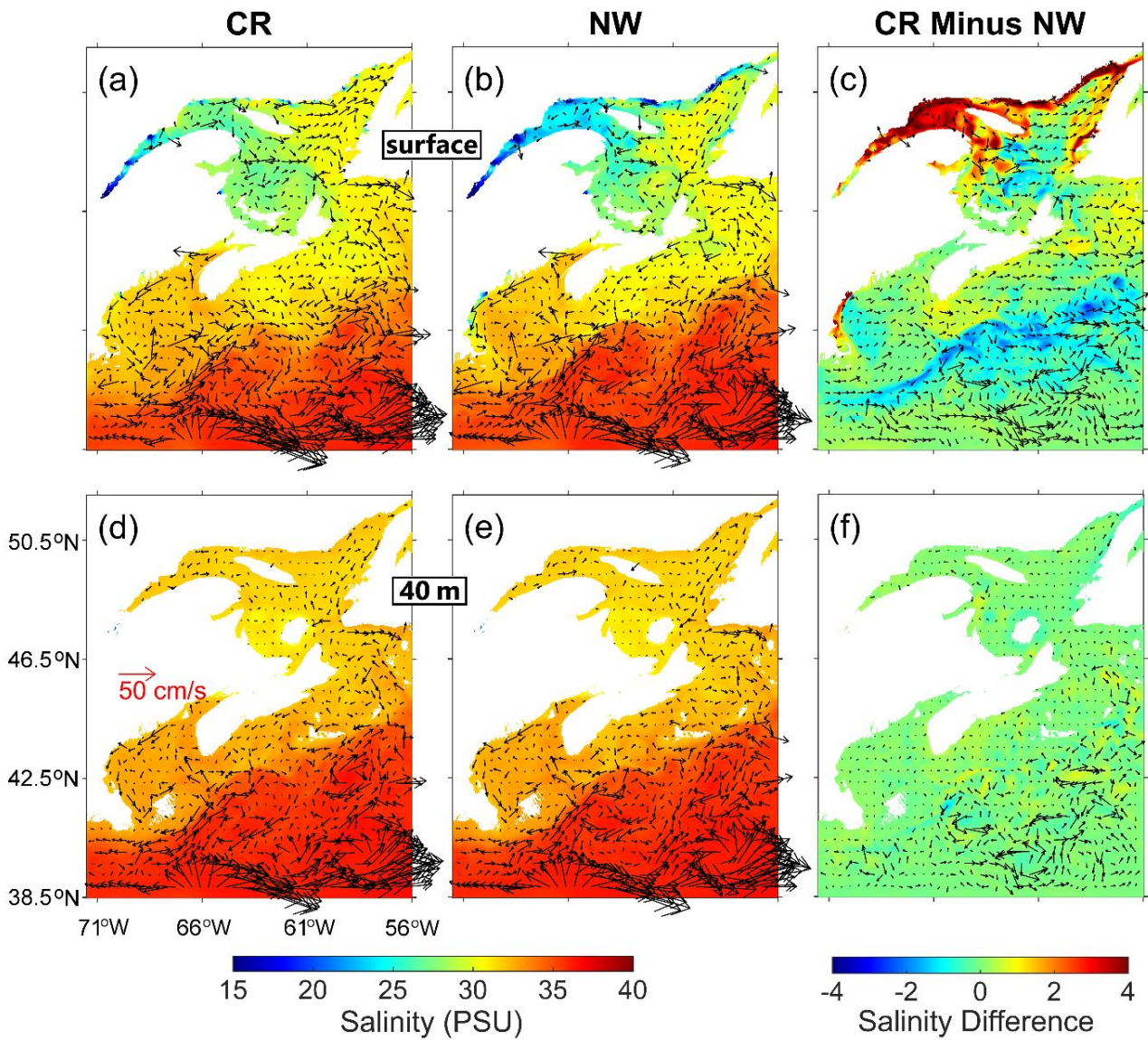


**Figure 11.** Monthly-mean currents and salinity in August 2018 produced by submodel L2 at (a,b) the sea surface and (d,e) the 40-m depth over the L2 domain in cases (a,d) CR and (b,e) NW. Differences in salinity and currents between cases CR and NW at (c) sea surface and (f) 40 m. For clarity, velocity vectors are plotted at every 14th model grid point. The current velocity vectors are identical to those shown in Figure 9.

The August-mean SSS ( $\bar{S}_0^{NW}$ ; Figure 11b) in case NW is relatively low and varies between 22 and 28 over the western GSL and coastal waters around CBI. This can be explained by the fact that, without wind forcing, freshwater discharge from the SLR remains in the thin surface layer for a long time and spreads seaward. In this month,  $\bar{S}_0^{NW}$  is nearly uniform and  $\sim 32$  in the GoM, and between 30 and 32 over the central and southwestern ScS. At the shelf break of the ScS-GoM,  $\bar{S}_0^{NW}$  in this month has a well-defined frontal boundary, with high  $\bar{S}_0^{NW}$  over 35 in the offshore waters beyond the shelf break.

The August-mean sub-surface (40 m) salinity ( $\bar{S}_{40}^{NW}$ ; Figure 11e) in case NW in 2018 is horizontally uniform and  $\sim 33$  over shelf regions of the GSL, ScS, and GoM, and relatively

high of over 35 in the slope waters and adjacent deep ocean waters. There is a sharp salinity front at the shelf break (Figure 11e).

The differences in the August-mean SSS ( $\Delta\bar{S}_0^{CR-NW}$ ; Figure 11c) between cases CR and NW are significantly positive and about 4 over the northwestern GSL and inshore waters of the northern GSL, which indicates the important role of wind forcing in blending the low-salinity surface waters with high-salinity sub-surface waters over these areas. Over the ScS, GoM, and deep ocean waters,  $\Delta\bar{S}_0^{CR-NW}$  is also positive but small, about 1. Over the slope waters of the ScS-GoM,  $\Delta\bar{S}_0^{CR-NW}$  is mostly negative. By comparison, the differences in the August-mean sub-surface salinity ( $\Delta\bar{S}_{40}^{CR-NW}$ ; Figure 11f) between cases CR and NW are relatively small over the whole L2 domain, particularly over the shelf regions.

Over the slope water region off the ScS-GoM,  $\Delta\bar{S}_0^{CR-NW}$  in August 2018 features a noticeable negative-value zone (Figure 11c). To further demonstrate the role of wind forcing in generating the negative values of  $\Delta\bar{S}_0^{CR-NW}$  over this slope region, we examine the August-mean salinity in cases CR ( $\bar{S}_{PQ}^{CR}$ ) and NW ( $\bar{S}_{PQ}^{NW}$ ) along transect PQ (marked in Figure 1b), which is a cross-shelf transect over the swScS. Distributions of  $\bar{S}_{PQ}^{CR}$  and  $\bar{S}_{PQ}^{NW}$  in the top 80 m along transect PQ in August 2018 are shown in Figure 12a,b. The salinity front in the top 20 m is broader over the slope portion of the transect (between 41.5 ° N and 42.8 ° N; Figure 12c) in case CR than in case NW (Figure 12a,b), which is mainly due to the effect of wind forcing on the seaward transport of coastal waters in case CR. As a result,  $\bar{S}_0^{CR}$  (Figure 12a) is lower than  $\bar{S}_0^{NW}$  (Figure 12b) over the slope region of transect PQ in August 2018. For the same reason, negative values of  $\Delta\bar{S}_0^{CR-NW}$  also occur over other slope waters to the south of the ScS and GoM in the summer months (Figure 11c).

Vertical profiles of the monthly-mean temperature and salinity in February and August 2018 on transect PP' (Figure 1c) produced by submodel L3 in cases CR and NW ( $\bar{T}_{PP}^{CR}, \bar{T}_{PP}^{NW}, \bar{S}_{PP}^{CR}, \bar{S}_{PP}^{NW}$ ) are analyzed to examine the role of winds in the vertical stratification over the swScS. In February 2018, both  $\bar{T}_{PP}^{CR}$  and  $\bar{S}_{PP}^{CR}$  (Figure 13a,c) have a three-layer vertical structure with a cold (<5 °C) and fresh (<32) surface layer in the top ~40 m, a relatively warmer (between 5 °C and 7 °C) and saltier (between 32 and 33) intermediate layer at depths between 40 m and 100 m, and a warm (>7 °C) and salty (>33.5) bottom layer at depths below 100 m. As mentioned earlier, strong winter convection is responsible for the nearly uniform vertical stratification in the surface mixed layer in this month in case CR (also reduces the upper-column vertical stratification in case NW). Wang et al. [9] demonstrated that the Nova Scotia Current splits into two branches over the northern flank of LaHave Basin: a narrow inshore branch (southwestward) over the inner shelf of the swScS and a broad offshore branch (meandering southward) over the western portion of LaHave Basin. The offshore branch of the Nova Scotia Current transports relatively cool and low-salinity upper-column waters seaward and crosses transect PP' at the middle, resulting in the relatively cool (~4 °C) and low-salinity (~31) waters in the top ~40 m in the middle section of the transect.

In case NW, by comparison, the vertical stratification of  $\bar{T}_{PP}^{NW}$  and  $\bar{S}_{PP}^{NW}$  (Figure 13b,d) in the top ~40 m in February 2018 is noticeably stronger than the counterpart in case CR, indicating the important role of wind-induced vertical mixing. In addition to vertical mixing, winds also affect the hydrography over the swScS through wind-induced modulation of circulation. Both  $\Delta\bar{U}_0^{\rightarrow CR-NW}$  and  $\Delta\bar{U}_{40}^{\rightarrow CR-NW}$  (Figure 8c,f) are northeastward in the inner ScS, and strong and offshore over the western portion of LaHave Basin. This implies the modulation effect of winds on the Nova Scotia Current in February 2018 counteract the inshore branch and enhance the offshore branch of the Nova Scotia Current, which also contributes to the differences between  $\bar{T}_{PP}^{CR}$  and  $\bar{T}_{PP}^{NW}$  and between  $\bar{S}_{PP}^{CR}$  and  $\bar{S}_{PP}^{NW}$  in this month.

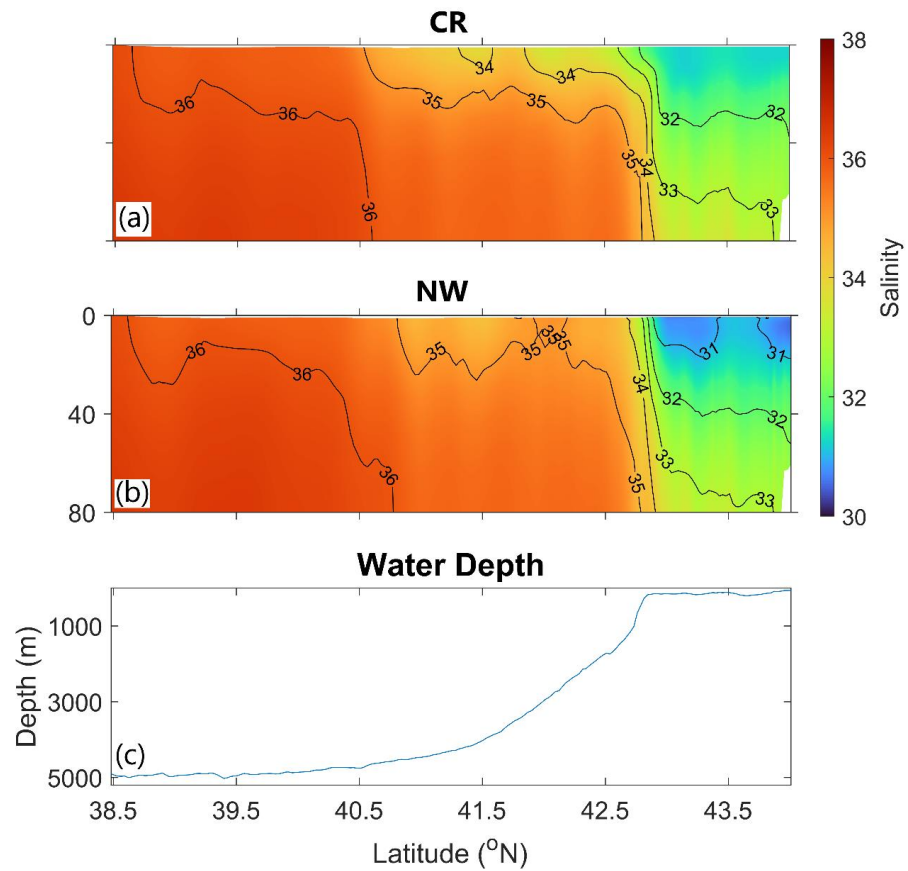


**Figure 12.** Vertical distributions of monthly-mean salinity for August 2018 in the top 80 m simulated by submodel L2 in cases (a) CR and (b) NW along cross-shelf transect PQ (shown in Figure 1b), and (c) profile of local water depths along transect PQ.

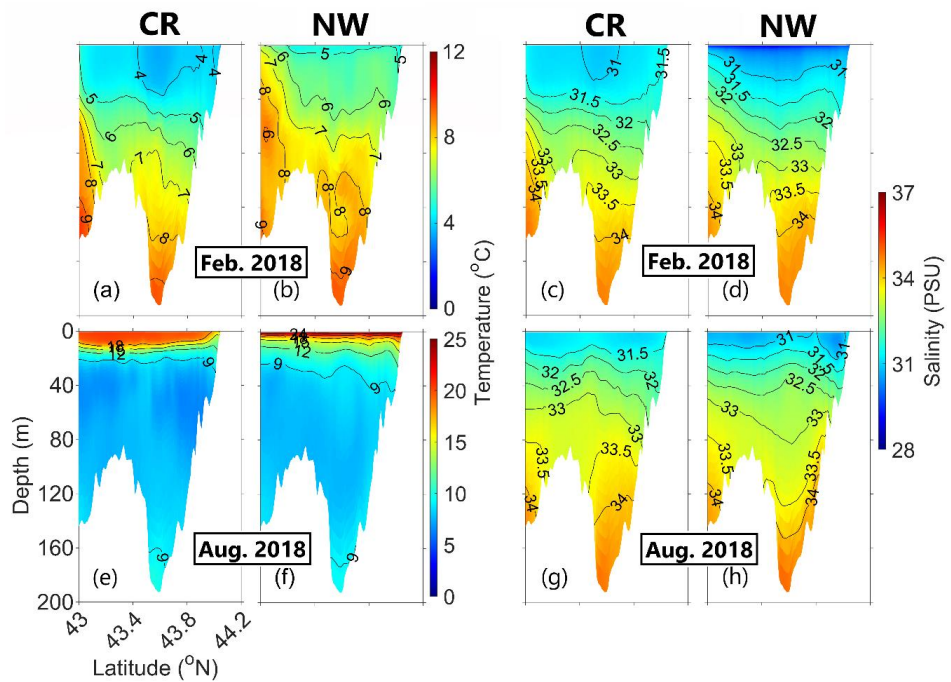


**Figure 13.** Vertical profiles of monthly-mean (a,b,e,f) temperature and (c,d,g,h) salinity in (a–d) February and (e–h) August 2018 produced by submodel L3 along transect PP' (shown in Figure 1c) in cases (a,c,e,g) CR and (b,d,f,h) NW.

In August 2018,  $\bar{T}_{PP}^{CR}$  and  $\bar{S}_{PP}^{CR}$  in case CR (Figure 13e,g) show a three-layer vertical structure, consisting of a warm ( $>18\text{ }^\circ\text{C}$ ) and fresh ( $<31.5$ ) surface layer in the top  $\sim 10$  m, a relatively cool ( $\sim 6\text{ }^\circ\text{C}$ ) and fresh (between 32 and 33) intermediate layer between 20 m and 80 m, and a warmer (between  $8\text{ }^\circ\text{C}$  and  $9\text{ }^\circ\text{C}$ ) and saltier ( $>33$ ) bottom layer below 80 m. This three-layer structure of hydrography is normally well-established between the late spring and early autumn [1]. The August-mean thermocline along transect PP' in case CR is nearly horizontal and at depths of about 10 m over the middle shelf of the transect (beyond  $\sim 50$  km away from the coast), tilts up over the inner shelf, and reaches the surface near the coast (Figure 13e). The tilts of the August-mean thermocline and 31.5-salinity layer over the inner shelf in case CR (Figure 13e,g) are associated by coastal upwelling induced by upwelling-favorable (northeastward) winds in the summer months.

The August-mean thermohaline on transect PP' in case NW is unrealistically too shallow over the middle of the transect (Figure 13f), due to the absence of wind-induced vertical mixing. Furthermore, the August-mean thermohaline in case NW does not tilt up over the inner shelf due to the absence of wind-induced upwelling. Below 30 m,  $\bar{T}_{PP}^{NW}$  and  $\bar{S}_{PP}^{NW}$  (Figure 13f,h) also have vertical distributions considerably different from the counterparts in case CR (Figure 13e,g) in August 2018. These differences (below 30 m, in August 2018) are partially associated with wind-induced modulation of baroclinic hydrodynamics. The shelf waves excited by winds in submodel L2 are present in case CR, but absent in case NW, also contributing to the differences between  $\bar{T}_{PP}^{CR}$  and  $\bar{T}_{PP}^{NW}$  and between  $\bar{S}_{PP}^{CR}$  and  $\bar{S}_{PP}^{NW}$  in August 2018.

To quantify the effects of winds on the monthly-mean currents over the swScS, we calculate the impact index ( $W_i^D$ ) of wind forcing at depth  $D$  ( $D$  equals 0 and 40 at the sea surface and the subsurface of 40 m, respectively) based on the L3 model results using the method by Wang et al. [9].

$$W_i^D = \frac{\left| \overset{\rightarrow}{U}_D^{CR} - \overset{\rightarrow}{U}_D^{NW} \right|}{\left| \overset{\rightarrow}{U}_D^{CR} \right| + \left| \overset{\rightarrow}{U}_D^{NW} \right|} \quad (1)$$

In February 2018, the values of  $W_i^0$  (Figure 14a) are large in the inner swScS mainly due to the northeastward wind-driven currents. The large values of  $W_i^0$  in the middle shelf are mainly associated with the wind-induced modulation of nonlinear circulation features, with contributions from wind-driven currents (e.g., eastward  $\overset{\rightarrow}{\Delta U}_0^{CR-NW}$  in the southwestern and southeastern portions of the swScS). In this month, the values of sub-surface (40 m) impact index ( $W_i^{40}$ ; Figure 14b) are highly comparable to their counterparts at the sea surface ( $W_i^0$ ; Figure 14a), except for the relatively smaller magnitudes at the sub-surface (40 m) than at the sea surface. The high similarities between  $W_i^0$  and  $W_i^{40}$  in February 2018 can be mainly explained by the strong vertical mixing and weak vertical stratification over the swScS in winter.

In August 2018, the wind-driven currents are northeastward and oppose the inshore branch of the Nova Scotia Current in the surface mixed layer over the inner swScS. In the middle shelf of the swScS, winds generate the eastward wind-driven transport and modulate the fine-scale gyres (Figure 14c) in the surface mixed layer in this month, resulting in the large values of  $W_i^0$  over the middle shelf. In August 2018, the values of  $W_i^{40}$  (Figure 14d) in the sub-surface (40 m) significantly differ from their counterparts at the sea surface. This can be mainly explained by the weak vertical mixing and strong vertical stratification over the swScS in the summer months. The large values of  $W_i^{40}$  over the inner and middle shelves of the swScS are mainly associated with the wind-induced modulation of gyres and the propagation of shelf waves excited by winds in submodel L2.



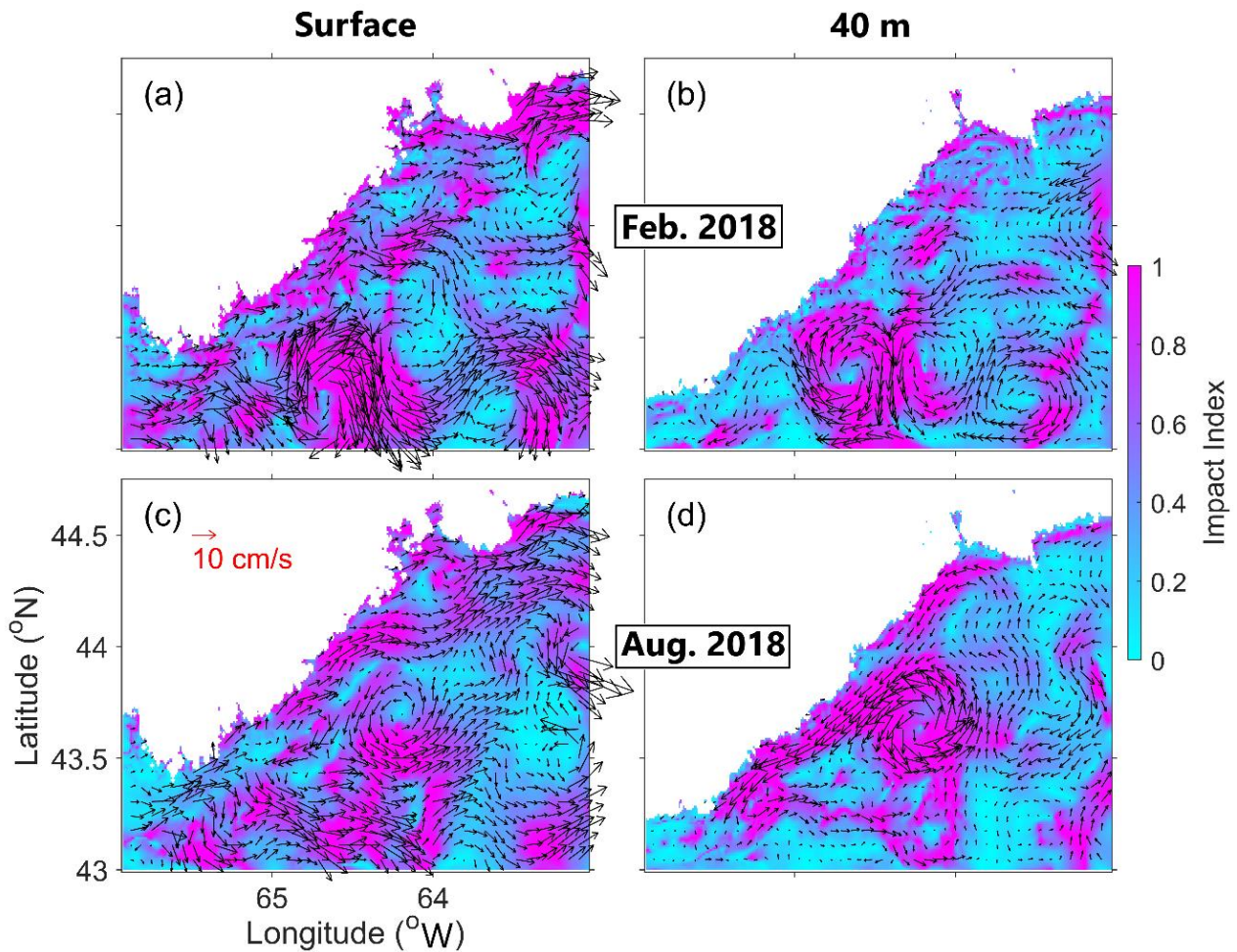


**Figure 14.** Differences in the monthly-mean (a,c) surface and (b,d) sub-surface (40 m) currents (vector fields) in (a,b) February and (c,d) August 2018 between cases CR and NW (calculated based on the L3 model results). For clarity, velocity vectors are plotted at every 7th model grid point. The color image indicates the associated impact index calculated using the method by Wang et al. [9].

#### 4.2. Effects of Tidal Forcing

The role of tidal forcing on 3D circulation and hydrography over the GSL-ScS-GoM region and adjacent deep waters is examined based on the differences in model results between cases CR and NT. The tidal forcing is excluded in the latter case (Table 1). In February 2018, the differences in the monthly-mean currents, temperature, and salinity at the sea surface ( $\Delta \bar{U}_0^{\rightarrow CR-NT}$ ,  $\Delta \bar{T}_0^{CR-NT}$ ,  $\Delta \bar{S}_0^{CR-NT}$ ) and at 40 m ( $\Delta \bar{U}_{40}^{\rightarrow CR-NT}$ ,  $\Delta \bar{T}_{40}^{CR-NT}$ ,  $\Delta \bar{S}_{40}^{CR-NT}$ ) between cases CR and NT have large values in the deep ocean region off the ScS-GoM, due to tide-induced modulations of the Gulf Stream, eddies, and meanders (Figure 15). Tides also modify the intensities and locations of warm-core rings over the slope water region off the ScS-GoM, as shown by the large cyclonic and anticyclonic circulation differences  $\Delta \bar{U}_0^{\rightarrow CR-NT}$  and  $\Delta \bar{U}_{40}^{\rightarrow CR-NT}$  over the slope waters. As mentioned above, warm-core rings are associated with Gulf Stream instability processes related to the conversion between the potential energy and eddy kinetic energy. Tidal forcing affects these instability processes through tide-induced modulation of baroclinic dynamics.

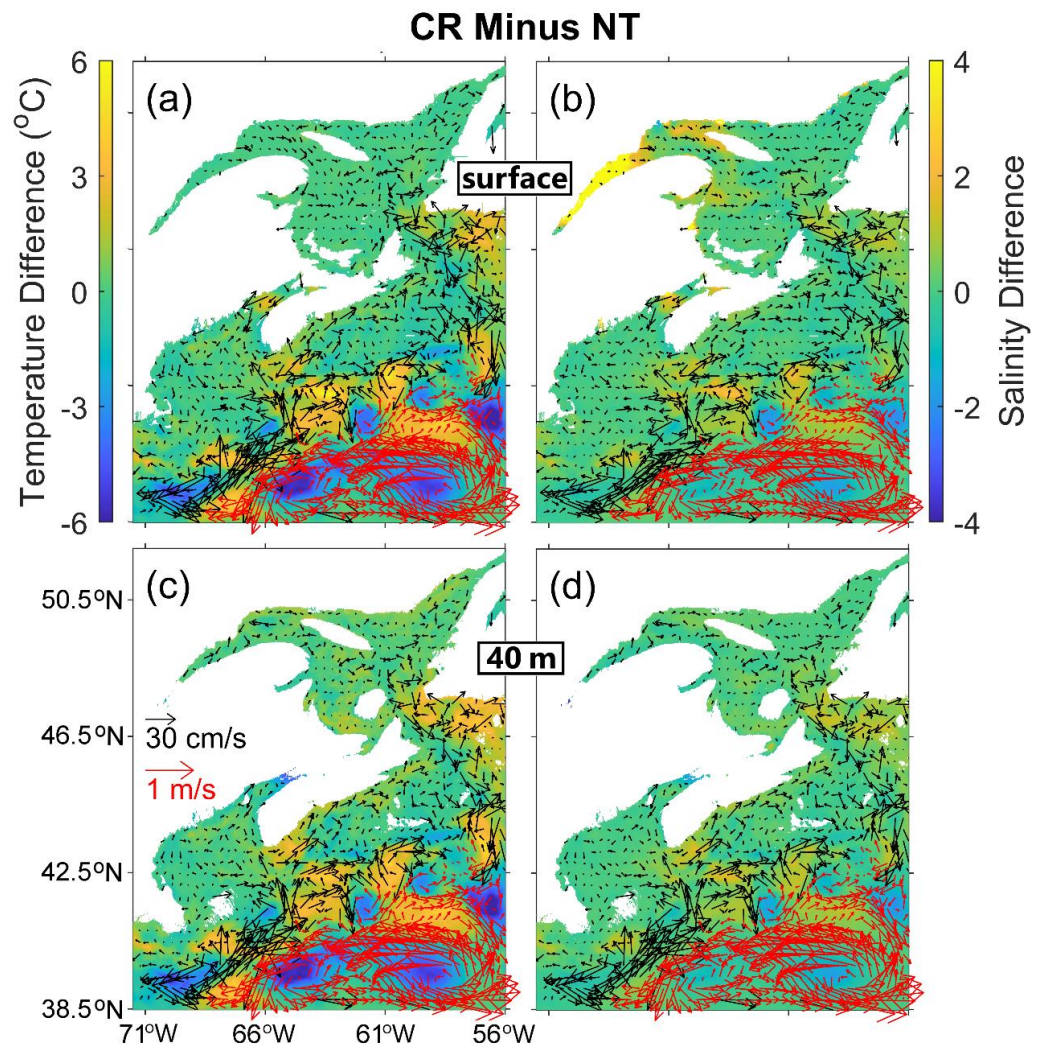


**Figure 15.** Differences in monthly-mean currents (black and red arrows), temperature (a,b), and salinity (c,d) simulated by submodel L2 for February 2018 between cases CR and NT at (a,b) the surface and (c,d) 40 m. For clarity, velocity vectors are plotted at every 12th model grid point. Different scales are used for the black and red arrows.

Over the inner shelf of the ScS in February 2018, tides modify the southeastward outflow from the southeastern GSL and induce relatively large (between  $0.1 \text{ m s}^{-1}$  and  $0.2 \text{ m s}^{-1}$ ) and northeastward  $\Delta \bar{U}_0^{\rightarrow CR-NT}$  and  $\Delta \bar{U}_{40}^{\rightarrow CR-NT}$  (Figure 15a,c). This indicates the important role of tide-induced horizontal advection over the ScS and southeastern GSL. Over coastal waters of the L2 domain, large values of  $\Delta \bar{T}_0^{CR-NT}$  and in this month occur only over several local areas with strong tidal mixing (e.g., the BoF), intense tide-induced upwelling (e.g., coastal waters to the south of Cape Sable Island), and significantly stratified upper-column temperature or salinity (e.g., the SLE, with significant salinity vertical stratification). The relatively large and northeastward currents of  $\Delta \bar{U}_0^{\rightarrow CR-NT}$  and  $\Delta \bar{U}_{40}^{\rightarrow CR-NT}$  over the inner shelf of the ScS in this month result in northeastward transport of relatively warm and salty waters (associated with strong tidal mixing and tide-induced topographic upwelling; Kim and Smith, 1993) along the coast of south Nova Scotia.

In August 2018, large values of  $\Delta \bar{U}_0^{\rightarrow CR-NT}$  and  $\Delta \bar{U}_{40}^{\rightarrow CR-NT}$  (Figure 16a,c) occur in the BoF, northern GoM, southwestern ScS, western GSL, and Cabot Strait, which are mainly density-driven currents associated with tide-induced modulations of local density

gradients. Some of these large  $\Delta \bar{U}_0^{\rightarrow CR-NT}$  and  $\Delta \bar{U}_{40}^{\rightarrow CR-NT}$  do not appear in February 2018 (e.g., in Cabot Strait and the northern GoM), mainly due to the strong convection and wind-induced mixing (resulting in typically small density gradients) in winter. The anticyclonic features of  $\Delta \bar{U}_0^{\rightarrow CR-NT}$  and  $\Delta \bar{U}_{40}^{\rightarrow CR-NT}$  around GeB (Figure 16a,c) are associated with tidal rectification [46]. The values of  $\Delta \bar{U}_0^{\rightarrow CR-NT}$  and  $\Delta \bar{U}_{40}^{\rightarrow CR-NT}$  around GeB are significantly larger in summer than in winter due to the reduced friction resulting from the weaker wind stress and stronger local density stratification in summer [46].

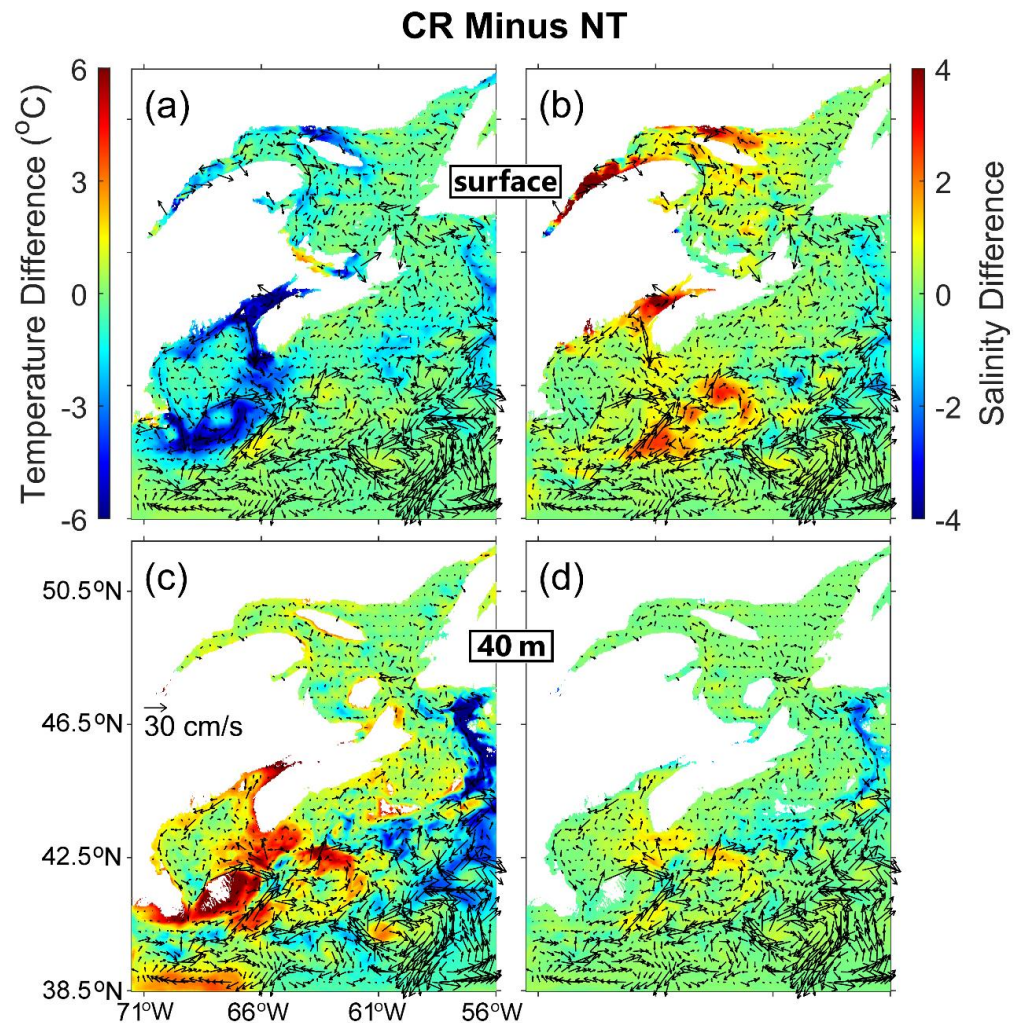


**Figure 16.** Differences in monthly-mean currents (black and red arrows), temperature (a,b), and salinity (c,d) simulated by submodel L2 for August 2018 between cases CR and NT at (a,b) the surface and (c,d) 40 m. For clarity, velocity vectors are plotted at every 11th model grid point. Different scales are used for the black and red arrows.

In August 2018, the tidal forcing reduces the August-mean SST over the BoF, coastal waters of the northern GoM, GeB and adjacent waters, and swScS, with negative and large values of  $\Delta T_0^{\rightarrow CR-NT}$  up to  $-7^\circ\text{C}$  (Figure 16a). Some noticeable SST cooling induced by tides also occurs in the northern GSL and the outer portion of the eastern ScS and adjacent waters. In summer, the large and positive net heat flux at the sea surface significantly warms the surface water and causes strong temperature vertical stratification in the top  $\sim 15$  m over the L2 domain. Strong tide-induced vertical mixing and tidal rectification are the main reason for the significant SST cooling (subsurface warming) shown in Figure 16a (Figure 16c), with some contribution from the horizontal transport of different water masses

by tide-induced mean currents. The tide-induced vertical mixing is also responsible for the large and positive values of  $\Delta \bar{S}_0^{CR-NT}$  over the coastal and shelf waters of the L2 domain (up to ~4; Figure 16b). In the deep waters off the ScS-GoM, there are small patches of positive and negative values of  $\Delta \bar{S}_0^{CR-NT}$  due to tide-induced modulations of the Gulf Stream, Labrador Current (inshore branch in the southwestern NFS and offshore branch along the shelf break of the eastern ScS), eddies, meanders, and rings. These tide-induced modulations are also responsible for the large and positive  $\Delta \bar{T}_{40}^{CR-NT}$  in the deep waters off the GoM and southwestern ScS, and for the large and negative values of  $\Delta \bar{T}_{40}^{CR-NT}$  over the southeastern portion of the Laurentian Channel and deep waters off the southeastern ScS (Figure 16c). In this month,  $\Delta \bar{S}_{40}^{CR-NT}$  is relatively small in the GSL and northeastern ScS, but relatively large and positive over the swScS (Figure 16d). The latter is associated with strong tidal mixing and tide-induced topographic upwelling [47]. In the deep waters off the swScS and GoM, small patches of positive  $\Delta \bar{S}_{40}^{CR-NT}$  occur mainly due to tide-induced modulations of fronts, eddies, and meanders.

To demonstrate the effect of tides on vertical stratification, we examine vertical profiles of monthly-mean temperature and salinity along the north-south transect EE' off Yarmouth (Figure 1c) based on model results produced by submodel L2 in cases CR ( $\bar{T}_{EE}^{CR}, \bar{S}_{EE}^{CR}$ ) and NT ( $\bar{T}_{EE}^{NT}, \bar{S}_{EE}^{NT}$ ). In both February and August 2018,  $\bar{T}_{EE}^{CR}$  and  $\bar{S}_{EE}^{CR}$  in case CR (Figure 17a,c,e,g) are vertically uniform in the whole water columns over the northern section (within 50 km from the coast) and weakly stratified over the southern section of the transect (beyond 50 km from the coast). Without tides in case NT,  $\bar{T}_{EE}^{NT}$  and  $\bar{S}_{EE}^{NT}$  in February 2018 are nearly uniform in the surface mixed layer along transect EE', mainly due to the strong winter convection caused by negative net heat flux and partially to the local wind-induced vertical mixing in the winter months (Figure 17b,d). At depths below 30 m over the southern section of the transect,  $\bar{T}_{EE}^{NT}$  and  $\bar{S}_{EE}^{NT}$  in case NT are relatively warm and salty in February 2018, due to the effect of warm-core eddy separated from the Gulf Stream. A comparison of monthly-mean hydrographic profiles in February 2018 in cases CR and NT (Figure 17a–d) indicates strong tide-induced vertical mixing at transect EE', particularly over the northern section of the transect.

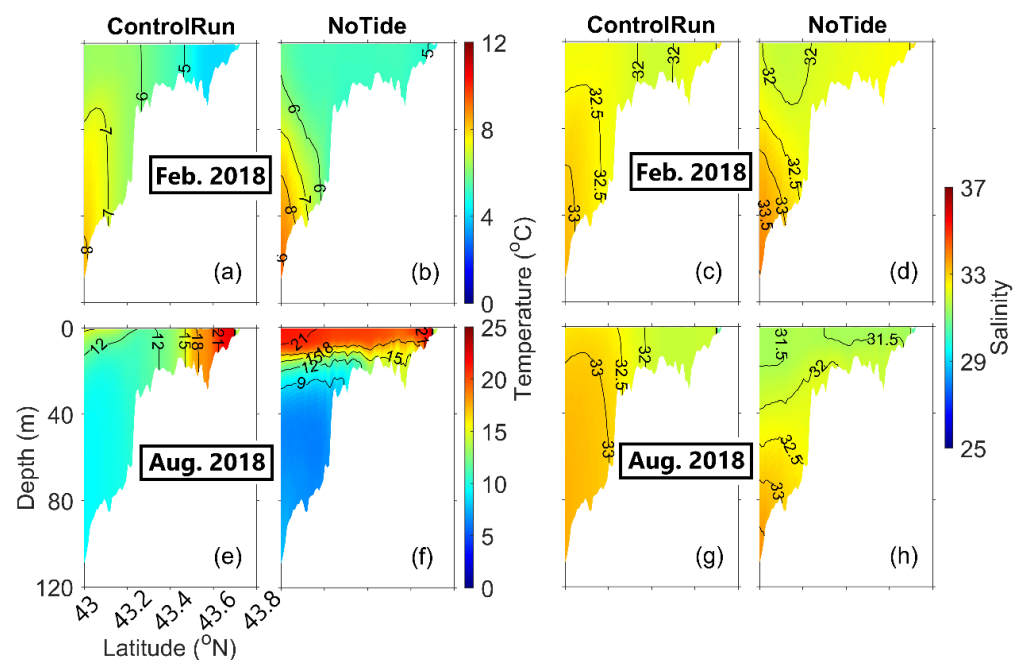


**Figure 17.** Vertical distributions of monthly-mean (a,b,e,f) temperature and (c,d,g,h) salinity in (a–d) February and (e–h) August 2018 along transect EE' (shown in Figure 1c) simulated by submodel L2 in (a,c,e,g) case CR and (b,d,f,h) case NT.

The August-mean  $\bar{T}_{EE}^{CR}$  and  $\bar{S}_{EE}^{CR}$  in 2018 in case CR (Figure 17e,g) are vertically uniform in the whole water columns over the northern section, and weakly stratified over the southern section of transect EE'. Without tides in case NT, the August mean  $\bar{T}_{EE}^{NT}$  and  $\bar{S}_{EE}^{NT}$  are highly stratified in the top 20 m (Figure 17f,h). The large differences in August-mean hydrography between cases CR and NT indicate the important role of strong tidal mixing in the vertical distributions of temperature and salinity over the inner and central shelves off Yarmouth. Over other areas with strong tides (e.g., the SLE and BoF), the vertical distributions of temperature and salinity are affected by tides in very similar ways.

To quantify the effects of tides on the monthly-mean currents over the swScS, we calculate the impact index ( $T_i^D$ ) of tides at depth  $D$  based on the L3 model results using the method by Wang et al. [9].

$$T_i^D = \frac{|\bar{U}_D^{\rightarrow CR} - \bar{U}_D^{\rightarrow NT}|}{|\bar{U}_D^{\rightarrow CR}| + |\bar{U}_D^{\rightarrow NT}|} \tag{2}$$

In February 2018, the values of  $T_i^{40}$  and  $\Delta \bar{U}_{40}^{\rightarrow CR-NT}$  at 40 m (Figure 18b) are highly comparable to their counterparts at the sea surface ( $T_i^0$  and  $\Delta \bar{U}_0^{\rightarrow CR-NT}$ ; Figure 18a). In particular,  $\Delta \bar{U}_0^{\rightarrow CR-NT}$  and  $\Delta \bar{U}_{40}^{\rightarrow CR-NT}$  in this month are mostly northeastward or offshore in the middle shelf of swScS, except for a few narrow strips. This can be mainly explained by the tide-induced horizontal transport and the modulation effect of tides on the Nova Scotia Current, as well as other nonlinear circulation features. The February-mean tide-induced transport in 2018 (Figure 15a,c) is generally northeastward over the swScS, weakening the alongshore (southwestward) transport of the Nova Scotia Current and thus enhancing its offshore transport (conservation of water mass). The values of  $T_i^0$  ( $T_i^{40}$ ) are large in the middle shelf of the swScS, particularly over the areas with large  $\Delta \bar{U}_0^{\rightarrow CR-NW}$  ( $\Delta \bar{U}_{40}^{\rightarrow CR-NT}$ ), quantifying the modulation effect of tides on the Nova Scotia Current and fine-scale gyres.

The August-mean  $\Delta \bar{U}_0^{\rightarrow CR-NT}$  (Figure 18c) in 2018 is large and westward to the south of Cape Sable Island, leading to a narrow strip of southwestward  $\Delta \bar{U}_0^{\rightarrow CR-NT}$  over the inner shelf in this month, which enhance the inshore branch of the Nova Scotia Current at the sea surface. The August-mean  $\Delta \bar{U}_0^{\rightarrow CR-NT}$  in 2018 also features a narrow strip of northeastward  $\Delta \bar{U}_0^{\rightarrow CR-NT}$  in the middle shelf of the swScS, and a strong and cyclonic gyre of  $\Delta \bar{U}_0^{\rightarrow CR-NT}$  over the southwestern portion of Emerald Basin (Figure 1c), indicating the tide-induced modulation in the offshore branch of the Nova Scotia Current. In the rest of the swScS, the large values of  $T_i^0$  in this month are mainly associated with the tide-induced modulation of fine-scale gyres and meanders. In August 2018,  $T_i^{40}$  and  $\Delta \bar{U}_{40}^{\rightarrow CR-NT}$  (Figure 18d) at the sub-surface (40 m) show some general similarities with their counterparts at the sea surface (Figure 18c) over most areas of the swScS, indicating that the tide-induced modulation in circulation occurs in the whole water column over the swScS.

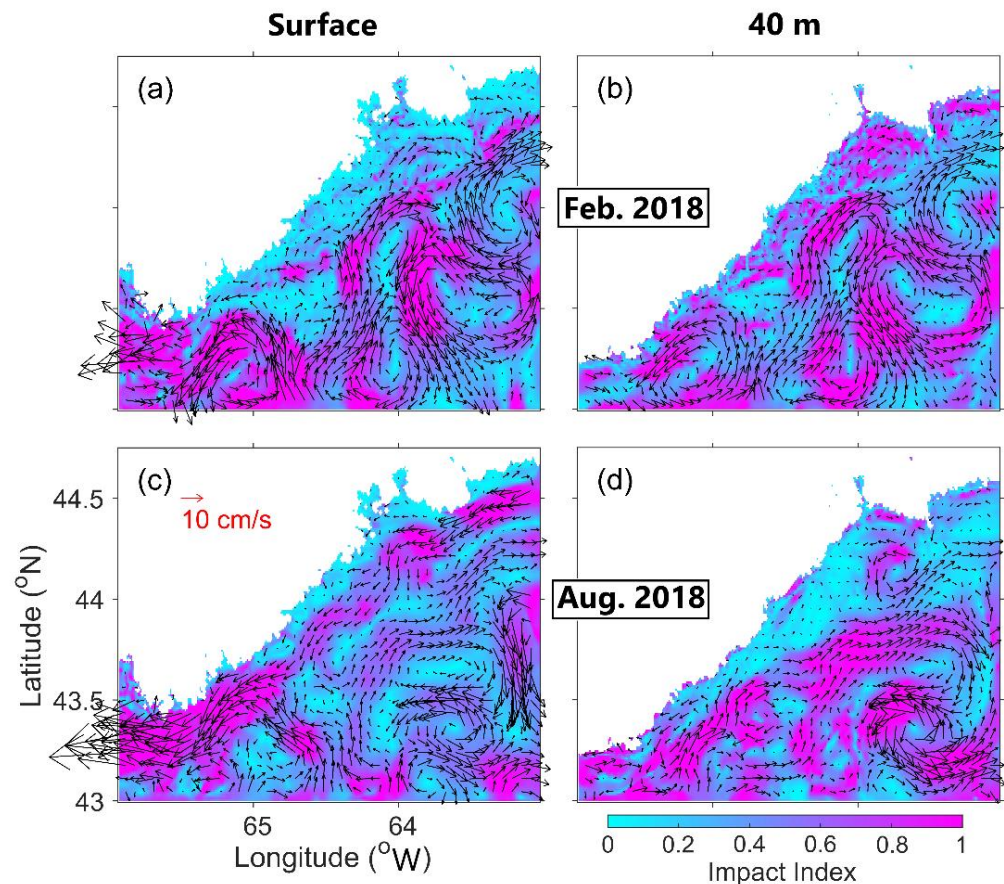


**Figure 18.** Differences in the monthly-mean (a,c) surface and (b,d) sub-surface (40 m) currents (vector fields) in (a,b) February and (c,d) August 2018 between cases CR and NT (calculated based on the L3 model results). For clarity, velocity vectors are plotted at every 7th model grid point. The color image indicates the associated impact index calculated using the method by Wang et al. [9].

## 5. Summary and Conclusions

A nested-grid circulation-ice modelling system for the southeastern Canadian Shelf (NGMS-seCS) was used in examining the variability of circulation and hydrography over the southwestern Scotian Shelf (swScS). The NGMS-seCS uses a three-level nesting setup, with the outermost submodel (L1) for the seCS and the innermost submodel (L3) for the swScS. The NGMS-seCS was validated using available observations and reanalysis data. The model was found to have satisfactory skills in reproducing the hydrography, circulation, and sea level over the study regions. The model was also found to have satisfactory skills in simulating the seasonal cycle of SST.

Three numerical experiments were conducted using the NGMS-seCS, which were: the Control Run (CR, with realistic forcing), NW (without winds in submodels L2 and L3), and NT (without tides). Model results from these experiments were analyzed to investigate the effects of winds and tides on the 3D circulation and hydrography over the swScS.

Model results (produced by submodel L2) in cases CR and NW were analyzed to quantify the effects of winds on hydrography and circulation over the L2 model domain, i.e., the Gulf of St. Lawrence (GSL)-Scotian Shelf (ScS)-Gulf of Maine (GoM) region and adjacent deep waters. In the late fall and winter months, negative surface heat fluxes significantly reduce the upper column (top ~40 m) vertical stratification in the swScS due to strong winter convection. In the summer months, the surface heat fluxes significantly warm the surface waters, resulting in strong vertical stratification in the top ~20 m over the swScS. Wind-induced vertical mixing is typically strong in winter and typically weak in summer, which also significantly affects the hydrographic distribution in the upper

water column (~40 m in winter and ~10 m in summer) of the swScS. In particular, wind-induced vertical mixing warms (significantly reduces) the SST and cools (slightly warms) the subsurface (40 m) temperature over most coastal areas of the GSL-ScS-GoM region in winter (summer). Wind-induced vertical mixing also increases the SSS over most of this region. In the winter (summer) months, wind forcing reduces (increases) the local SST over Georges Bank (GeB), the Bay of Fundy (BoF), and the inner shelf off Yarmouth mainly through latent and sensible heat fluxes, with additional contributions from wind-induced horizontal mixing and advection. Wind-induced horizontal mixing and advection also enhance the seaward propagation of low-salinity estuarine waters over coastal areas of the GSL-ScS-GoM. Winds also modify the eddies and meanders over the swScS through wind-induced modulations of baroclinic hydrodynamics and wind-driven currents.

Model results in cases CR and NT indicated the important role of tidal forcing in 3D circulation and hydrography over the GSL-ScS-GoM and adjacent deep waters. In the winter months, tides increase the SST over the BoF and coastal waters of the swScS and increase the SSS over the SLE, BoF, and swScS. Tides also generate the northeastward transport of relatively warm and salty waters (originating from the swScS) along the south coast of Nova Scotia, modulating the Nova Scotia Current and nonlinear circulation features over the swScS. Over the BoF, northern GoM, swScS, western GSL, and Cabot Strait, tide-induced modulations of local density gradients result in large density-driven currents in summer months. Strong tidal mixing and tidal rectification also significantly reduces the SST, increase the SSS, and increase subsurface temperature in the BoF, coastal waters of the northern GoM, GeB and adjacent waters, and coastal waters of the swScS in the summer months. In deep waters off the ScS-GoM, tidal forcing also modifies the Gulf Stream, eddies, meanders, and warm/cold-core rings through tide-induced modulation of baroclinic hydrodynamics.

This study sought to further our understanding of the 3D circulation and hydrography over the Scotian Shelf and surrounding areas through numerical experiments designed to identify the roles of winds and tides. In a future study, we plan to study the relationship between the physical and biogeochemical states of the Scotian Shelf waters by coupling the L3 submodel to a simple oxygen model. Additional future research is needed on the interaction between tides and currents (e.g., the Gulf Stream), which is indicated in the differences between simulations with and without tides. The numerical simulation results of Wang et al. [9] indicated that internal tides are generated near the southwestern end of the Scotian Shelf and propagate offshore. A detailed study of the internal tides in this region and their interaction with subtidal flows, as has been done for the Mid-Atlantic Bight by Kelly and Lermusiaux [48], would provide further insights into the dynamics of the Scotian Shelf and adjacent waters.

**Author Contributions:** Conceptualization, Q.P., J.S. and K.O.; methodology, Q.P., J.S. and K.O.; formal analysis, Q.P., J.S. and K.O.; writing—original draft preparation, Q.P.; writing—review and editing, Q.P., J.S. and K.O. All authors have read and agreed to the published version of the manuscript.

**Funding:** This study was supported by the Natural Sciences and Engineering Research Council of Canada, the Ocean Frontier Institute, and the Marine Environmental Observation, Prediction, and Response Network.

**Data Availability Statement:** Publicly available datasets were used in this study. These datasets can be found here: <https://podaac.jpl.nasa.gov/>; <https://catalogue.ceda.ac.uk/>; <https://www.tpxo.net/>; <https://isdmgdsi.gc.ca/>, accessed on 5 October 2022.

**Acknowledgments:** The authors wish to thank Jonathan Grant, Eric Oliver, Li Zhai, and David Greenberg for their constructive comments and suggestions. This study utilized computational resources maintained by Compute Canada (now the Digital Research Alliance of Canada).

**Conflicts of Interest:** The authors declare no conflict of interest.

## Appendix A. List of Abbreviations and Symbols Used

### Appendix A.1. Abbreviations

3D	Three-dimensional
BoF	Bay of Fundy
CBI	Cape Breton Island
CCI	Climate Change Initiative
CICE	Los Alamos Sea Ice Model
CMC	Canadian Meteorological Center
CR	Control run
ECS	eastern Canadian shelf
ECV	Essential Climate Variable
ESA	European Space Agency
GB	Grand Banks
GDS	GHRSSST Data Processing Specification
GeB	Georges Bank
GEBCO	General Bathymetric Chart of the Oceans
GHRSSST	Group for High Resolution Sea Surface Temperature
GLORYS	Global Ocean Physics Reanalysis
GoM	Gulf of Maine
GSL	Gulf of St. Lawrence
ICOADS	International Comprehensive Ocean-Atmosphere Data Set
L1	Level one
L2	Level two
L3	Level three
LS	Labrador Shelf
NARR	North American Regional Reanalysis
NFS	Newfoundland Shelf
NGMS-seCS	Nested-grid modelling system for the southeastern Canadian Shelf
NoL3Wind	Wind forcing in submodel L3 turned off
NT	Tidal forcing turned off, otherwise identical to CR
NW	Wind forcing in submodels L2 and L3 turned off, otherwise identical to CR
OTIS	Oregon State University Tidal Inversion System
PEI	Prince Edward Island
PODAAC	Physical Oceanography Distributed Active Archive Center
ROMS	Regional Ocean Modeling System
ScS	Scotian Shelf
seCS	Southeastern Canadian Shelf
SLE	St. Lawrence Estuary
SLGO	St. Lawrence Global Observatory
SLR	St. Lawrence River
swScS	Southwestern ScS
SSS	Sea surface salinity
SST	Sea surface temperature

### Appendix A.2. Symbols

$N^2$	Brunt–Väisälä frequency square
$r^2$	Correlation square
$T_{\bar{A}} (T_{\bar{B}})$	Temperature averaged over green box A (B) in Figure 1b.
$T_i^D$	Impact index of tides at depth D
$\Delta \bar{T}_Y^{C1-C2}$	Monthly-mean temperature difference between cases C1 and C2 at the depths of Y meters (0 represents the sea surface)
$S_{\bar{A}} (S_{\bar{B}})$	Salinity averaged over green box A (B) in Figure 1b.
$\sigma$	Standard deviation
$\Delta \bar{S}_Y^{C1-C2}$	Monthly-mean salinity difference between cases C1 and C2 at depths of Y meters (0 represents the sea surface)
$\vec{U}_D^{C1}$	Monthly-mean currents at depth D in case C1



$\vec{\Delta U}_Y^{C1-C2}$	Monthly-mean circulation difference (two-dimensional vector field) between cases C1 and C2 at the depths of Y meters
$\Delta \bar{U}_{PP}^{CR-NT}$ & $\Delta \bar{V}_{PP}^{CR-NT}$	Monthly-mean alongshore (northeastward) and onshore Current differences between cases Control Run and NoTide along transect PP' (shown in Figure 1c)
$W_i^D$	Impact index of winds at depth D
$\beta$	Coefficient for semi-prognostic method
$\gamma^2$	Metric to assess model performance (defined in Appendix G)
$\theta$	Coefficient for sponge layer nudging
$Var()$	Variance
$z$	Vertical Cartesian coordinate
$z_0$	Thickness of bottom boundary layer in the parameterization of bottom friction

### Appendix B. Parameterization of Bottom Friction

The logarithmic parameterization of bottom friction is used in this study. This parameterization assumes that currents have the classic vertical logarithmic profile in the bottom boundary layer:

$$|u| = \frac{u_*}{\kappa} \ln\left(\frac{z}{z_0}\right) \tag{A1}$$

where  $|u| = \sqrt{u^2 + v^2}$  is the current speed,  $u_* = \sqrt{|\tau_{bx}| + |\tau_{by}|}$  is the friction velocity,  $\tau_{bx}$  and  $\tau_{by}$  are components of kinematic bottom stress,  $z$  is the elevation above the sea bottom,  $\kappa = 0.41$  is the von Karman constant,  $z_0$  is the bottom roughness length (set to 0.02 m in this study).

The kinematic stress is parameterized as

$$\tau_{bx} = \frac{\kappa^2 u \sqrt{u^2 + v^2}}{\ln^2\left(\frac{z}{z_0}\right)} \tag{A2}$$

$$\tau_{by} = \frac{\kappa^2 v \sqrt{u^2 + v^2}}{\ln^2\left(\frac{z}{z_0}\right)} \tag{A3}$$

The parameterization for the bottom friction can be found in Warner et al. [29].

### Appendix C. Sponge Layer Nudging

In submodel L1, a thin sponge layer (with a thickness of 20 grid points) is defined along each lateral boundary in which the model temperature and salinity are nudged toward the daily GLORYS 12V1 reanalysis values as:

$$X_A = X_U + \theta \Delta(X_{GLO} - X_U) \tag{A4}$$

where  $X_A$  is the adjusted temperature or salinity,  $X_U$  is the prognostic temperature or salinity, and  $X_{GLO}$  is the reanalysis temperature or salinity. In this study,  $\theta$  is set to  $0.5 \text{ day}^{-1}$  in the 15 grid points closest to the model boundary and decreases linearly to 0 in the next 5 grid points.

### Appendix D. Semi-Prognostic Method

In the semi-prognostic method, the model hydrostatic equation

$$\frac{\partial P}{\partial z} = -g\rho_m \tag{A5}$$

is adjusted to

$$\frac{\partial P}{\partial z} = -g[\rho_m + \beta(\rho_C - \rho_m)] \tag{A6}$$

where  $\rho_m$  is the prognostic density,  $\rho_c$  is the density calculated from the climatological temperature and salinity, and  $\beta$  is the nudging coefficient. The coefficient  $\beta$  is set to 0.15 in this study. The operator  $\overline{(\ )}$  denotes spatial averaging.

The semi-prognostic method introduces a correction term  $-\frac{1}{\rho_0} \nabla \hat{P}$  to the horizontal momentum equations, where  $\hat{P}$  satisfies

$$\frac{\partial \hat{P}}{\partial z} = -g\beta \overline{(\rho_c - \rho_m)} \tag{A7}$$

with  $\hat{P} = 0$  at  $z = 0$ . This correction term modifies the simulated circulation, and thus indirectly alters the simulated temperature and salinity. More details of the semi-prognostic method are available in Sheng et al. [25].

### Appendix E. The Spectral Nudging Method

In the spectral nudging method, the model-computed temperature and salinity are nudged toward the climatological temperature and salinity values at certain frequency bands. Using temperature as an example, the tracer equation with spectral nudging is:

$$\frac{\partial T}{\partial t} + (\mathbf{u} \cdot \nabla) T = A \cdot \nabla^2 T + \gamma \langle T_c - T \rangle \tag{A8}$$

where the nudging term

$$\langle T_c - T \rangle = \int_{-\infty}^0 \phi(\tau) [T_c(t + \tau) - T(t + \tau)] d\tau \tag{A9}$$

is a weighted average of previous differences between the climatological and prognostic temperatures,  $\gamma$  is a coefficient controlling the strength of the nudging,  $\phi(\tau)$  is a weighting function that controls the frequencies at which the nudging is applied,  $T$  is the prognostic temperature,  $T_c$  is the climatological temperature, and  $\mathbf{u}$  is the 3D velocity vector. More details of the spectral nudging method are available in Thompson et al. [26]. In this study,  $\gamma$  for both temperature and salinity is 0 between the sea surface and the 30-m depth, linearly increases from 0 to 0.0011 between depths of 30 and 40 m, and is 0.0011 at depths greater than 40 m.

### Appendix F. Validation of Sea Ice Concentration

Figure A1a shows the monthly-mean sea ice concentration (represented as a fraction of model grid point area) in February 2018 simulated by submodel L1. Model results feature high sea ice concentration over the LS, northeastern NFS, the SLE, Strait of Belle Isle, and coastal waters off western PEI. Over these areas, the local ice production is large in the winter months due to strong negative heat flux (i.e., net heat loss from the ocean surface to the atmosphere) and relatively low SSS in comparison with other areas of the seCS. The freezing point is higher for lower salinity waters, leading to more local ice production. Urrego-Blanco and Sheng [49] demonstrated that both thermodynamics and ice dynamics play important roles in affecting the sea ice concentration in the GSL. Furthermore, over the LS and northern NFS, the sea ice conditions are also affected by the southward advection of some Arctic and sub-Arctic sea ice carried by the Labrador Current in the winter months [50,51].

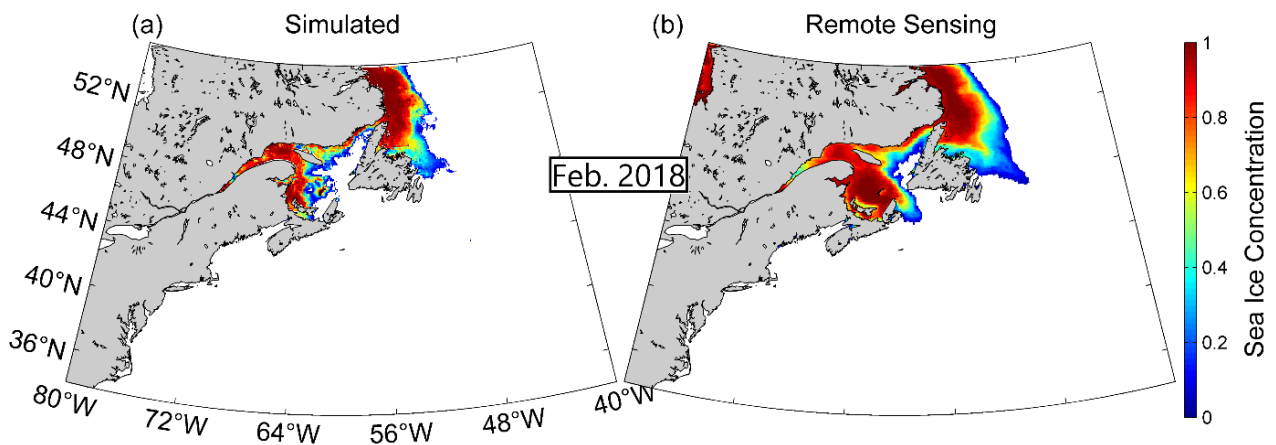


**Figure A1.** Monthly-mean sea ice concentration (as a fraction of model grid point area) in February 2018 (a) produced by NGMS-seCS and (b) from the daily GHRST Level 4 CMC0.1deg Global Foundation Sea Surface Temperature Analysis (GDS version 2) dataset over the domain of submodel L1.

As shown in Figure A1, submodel L1 has satisfactory skills in reproducing the observed monthly-mean sea ice concentrations over the LS, Strait of Belle Isle, northern GSL, and northeastern NFS. However, submodel L1 has large deficiencies in simulating the sea ice concentration over the southwest GSL and coastal waters off CBI and eastern PEI. The reasons for the large model deficiencies in simulating sea ice conditions are still under investigation. One possible reason is that the thermodynamics over these local areas may not be simulated well due to deficiencies in the parametrization of local vertical mixing. Another plausible reason is inaccuracies in the simulated net heat flux during the ice formation period.

**Appendix G. Definition of  $\gamma^2$**

The metric  $\gamma^2$  is defined by Thompson and Sheng [52] as:

$$\gamma^2 = \frac{Var(X_o - X_s)}{Var(X_o)} \tag{A10}$$

where  $X_S$  and  $X_O$  respectively represent the simulated and observed value of variable  $X$  at a given time. Smaller values of  $\gamma^2$  indicate better agreement between observed and simulated values of the variable  $X$ . Values of  $\gamma^2$  below 1 can be considered as indicators of good model performance.

**Appendix H. Seasonal Variability of the Vertical Stratification over the swScS**

To examine the seasonal variability of the vertical stratification in the swScS, the time series (produced by submodel L2) of temperature ( $T_{\bar{A}}$ ; Figure A2a), salinity ( $S_{\bar{A}}$ ; Figure A2b), and Brunt-Väisälä frequency square ( $\log_{10}(N_{\bar{A}}^2)$  in Figure A2c calculated based on  $T_{\bar{A}}$ ,  $S_{\bar{A}}$ , and pressure fields) averaged over green box A (Figure 1b) are analyzed. In the winter months, strong winter convection and wind-induced vertical mixing significantly reduce the vertical stratification in the top ~40 m over the swScS, as shown by the nearly uniform  $T_{\bar{A}}$  (~4°C) and  $S_{\bar{A}}$  (~31) in the top ~40 m in Figure A2a,b. During the same period, the values of  $\log_{10}(N_{\bar{A}}^2)$  are small (between -6 and -4) in the upper water column, indicating the small density gradients in the vertical in the surface mixed layer. Between 40 m and 80 m, the vertical stratification over the swScS in winter is relatively stronger than its counterpart in the surface mixed layer, with  $T_{\bar{A}}$  increasing from ~5.5 to ~7.5 with depth,  $S_{\bar{A}}$  increasing from ~31.5 to 33.5 with depth, and  $\log_{10}(N_{\bar{A}}^2)$  between -4 and -3.5. Below 140 m, the density gradients in the vertical are generally weak, with small values

of  $\log_{10}\left(N_A^2\right)$  about  $-4.5$ . Between early spring and late summer, the wind forcing over the swScS is generally much weaker than its counterpart in the winter months, and the positive surface heat fluxes gradually raise the upper-column (top  $\sim 20$  m) temperature. This results in the strong vertical stratification in the top  $\sim 20$  m over the swScS, with large values of  $\log_{10}\left(N_A^2\right)$  between  $-3$  and  $-2.5$ . Although wind-induced vertical mixing is much weaker in summer than in winter, it still noticeably reduces the vertical stratification in the top  $\sim 10$  m over the swScS in summer (as shown by the very small patches of small values of  $\log_{10}\left(N_A^2\right)$  in the top  $\sim 5$  m in the summer months). Between early autumn and early winter, the wind-induced vertical mixing over the swScS gradually increases (due to gradually increasing wind speed), and the upper column temperature gradually decreases (from  $\sim 18$  °C to  $\sim 5.5$  °C, due to negative surface fluxes). As a result of strong convection resulting from surface cooling and wind-induced vertical mixing, the upper-column vertical stratification in the swScS significantly decreases (with  $\log_{10}\left(N_A^2\right)$  decreases from  $\sim -3.5$  to  $\sim -6$ ), and the surface mixed layer depths over the swScS increase from  $\sim 10$  m to  $\sim 35$  m.

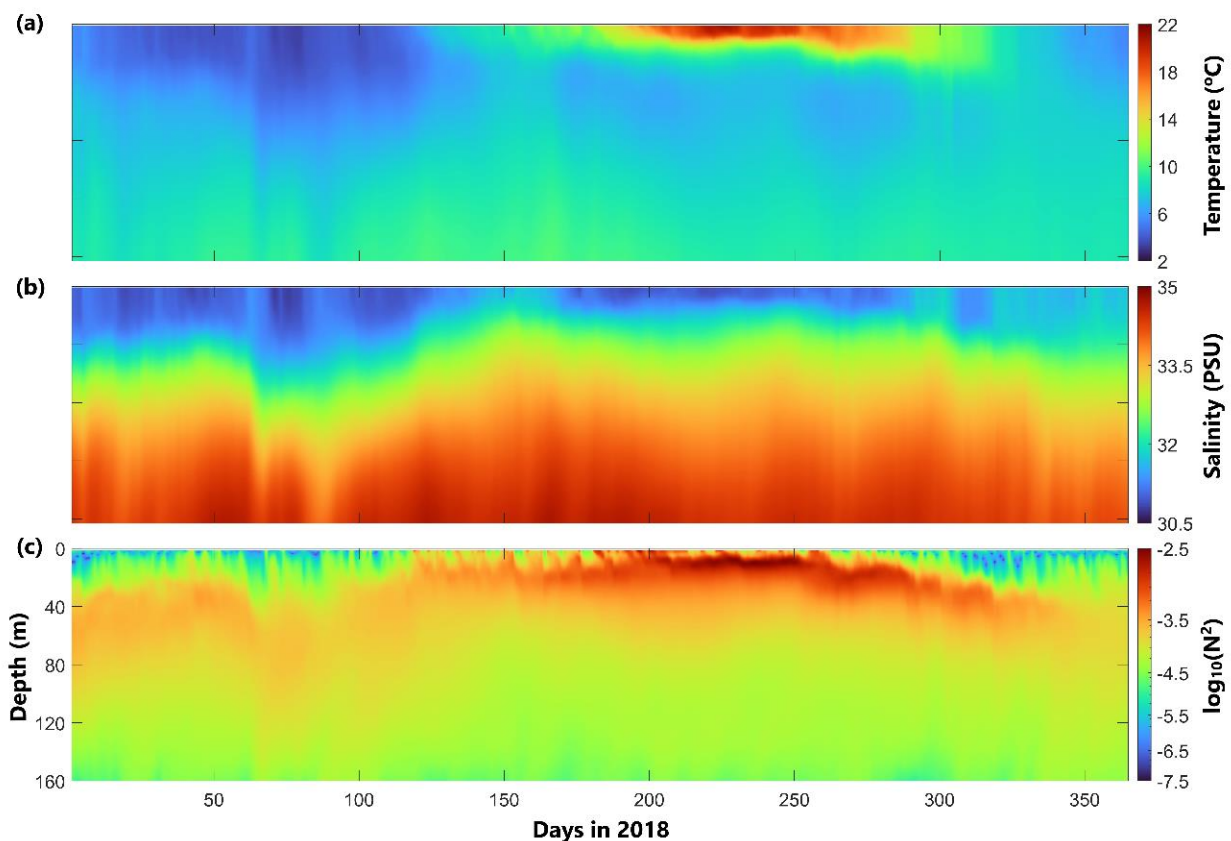


**Figure A2.** Time series of (a) temperature, (b) salinity, and (c)  $\log_{10}(N^2)$  averaged in green box A (Figure 1b, in the swScS) in 2018. The time series of temperature, salinity, and  $\log_{10}(N^2)$  are calculated based on the daily-mean model results produced by submodel L2.

## References

1. Smith, P.; Petrie, B.; Mann, C. Circulation, variability, and dynamics of the Scotian Shelf and slope. *Can. J. Fish. Aquat. Sci.* **1978**, *35*, 1067–1083. [[CrossRef](#)]
2. Han, G.; Hannah, C.; Loder, J.; Smith, P. Seasonal variation of the three-dimensional mean circulation over the Scotian Shelf. *J. Geophys. Res.* **1997**, *102*, 1011–1025. [[CrossRef](#)]
3. Schwing, F. Subtidal response of the Scotian Shelf bottom pressure field to meteorological forcing. *Atmos. Ocean* **1989**, *27*, 157–180. [[CrossRef](#)]
4. Schwing, F. Subtidal response of Scotian Shelf circulation to local and remote forcing. Part II: Barotropic model. *J. Phys. Oceanogr.* **1992**, *22*, 542–563. [[CrossRef](#)]

5. Greenberg, D.; Loder, J.; Shen, Y.; Lynch, D.; Naimie, C. Spatial and temporal structure of the barotropic response of the Scotian Shelf and Gulf of Maine to surface wind stress: A model-based study. *J. Geophys. Res.* **1997**, *102*, 20897–20915. [[CrossRef](#)]
6. Zhai, L.; Sheng, J.; Greatbatch, R. Application of a nested-grid ocean circulation model to Lunenburg Bay of Nova Scotia: Verification against observations. *J. Geophys. Res.* **2008**, *113*, C02024. [[CrossRef](#)]
7. Shan, S.; Sheng, J. Numerical study of topographic effects on wind-driven coastal upwelling on the Scotian Shelf. *J. Mar. Sci.* **2022**, *10*, 497. [[CrossRef](#)]
8. Smith, P. The mean and seasonal circulation off southwest Nova Scotia. *J. Phys. Oceanogr.* **1983**, *13*, 1034–1054. [[CrossRef](#)]
9. Wang, Y.; Sheng, J.; Lu, Y. Examining tidal impacts on seasonal circulation and hydrography variability over the eastern Canadian shelf using a coupled circulation-ice regional model. *Prog. Oceanogr.* **2020**, *189*, 102448. [[CrossRef](#)]
10. Yang, B.; Sheng, J. Process study of coastal circulation over the inner Scotian Shelf using a nested-grid ocean circulation model, with a special emphasis on the storm-induced circulation during tropical storm Alberto in 2006. *Ocean Dyn.* **2008**, *58*, 375–396. [[CrossRef](#)]
11. Ohashi, K.; Sheng, J.; Thompson, K.; Hannah, C.; Ritchie, H. Numerical study of three-dimensional shelf circulation on the Scotian Shelf using a shelf circulation model. *Cont. Shelf Res.* **2009**, *29*, 2138–2156. [[CrossRef](#)]
12. Chegini, F.; Lu, Y.; Katavouta, A.; Ritchie, H. Coastal upwelling off southwest Nova Scotia simulated with a high-resolution baroclinic ocean model. *J. Geophys. Res.* **2018**, *123*, 2318–2331. [[CrossRef](#)]
13. Hedström, K. *Technical Manual for a Coupled Sea-Ice/Ocean Circulation Model*; Version 3; U.S. Department of the Interior Bureau of Ocean Energy Management: Anchorage AK, USA, 2009; p. 158.
14. Hunke, E.; Lipscomb, W.; Jones, P.; Turner, A.; Jeffery, N.; Elliott, S. *CICE, The Los Alamos Sea Ice Model Version 00*; Los Alamos National Laboratory: Los Alamos, NM, USA, 2017.
15. Smagorinsky, J. General circulation experiments with the primitive equations: I. The basic experiment. *Mon. Weather Rev.* **1963**, *91*, 99–164. [[CrossRef](#)]
16. Mellor, G.; Yamada, T. Development of a turbulence closure model for geophysical fluid problems. *Rev. Geophys.* **1982**, *20*, 851–875. [[CrossRef](#)]
17. Egbert, G.; Erofeeva, S. Efficient inverse modeling of barotropic ocean tides. *J. Atmos. Ocean. Technol.* **2002**, *19*, 183–204. [[CrossRef](#)]
18. Mesinger, F.; DiMego, G.; Kalnay, E.; Mitchell, K.; Shafran, P.; Ebisuzaki, W.; Jović, D.; Woollen, J.; Rogers, E.; Berbery, E.; et al. North American regional reanalysis. *Bull. Am. Meteor. Soc.* **2006**, *87*, 343–360. [[CrossRef](#)]
19. Large, W.; Pond, S. Open ocean momentum flux measurements in moderate to strong winds. *J. Phys. Oceanogr.* **1981**, *11*, 324–336. [[CrossRef](#)]
20. Lin, S.; Sheng, J.; Ohashi, K.; Song, Q. Wave-current interactions during Hurricanes Earl and Igor in the northwest Atlantic. *J. Geophys. Res.* **2021**, *162*, e2021JC017609. [[CrossRef](#)]
21. Bourgault, D.; Koutitonsky, V. Real-time monitoring of the freshwater discharge at the head of the St. Lawrence Estuary. *Atmos. Ocean* **1999**, *37*, 203–220. [[CrossRef](#)]
22. Sheng, J.; Wang, L.; Andréfouët, S.; Hu, C.; Hatcher, B.; Muller-Karger, F.; Kjerfve, B.; Heyman, W.; Yang, B. Upper Ocean response of the Mesoamerican Barrier Reef System to Hurricane Mitch and coastal freshwater inputs: A study using Sea-viewing Wide Field-of-view Sensor (SeaWiFS) ocean color data and a nested-grid ocean circulation model. *J. Geophys. Res.* **2007**, *112*, C07016. [[CrossRef](#)]
23. Ji, X.; Sheng, J.; Tang, L.; Liu, D.; Yang, X. Process study of circulation and hydrography in the Pearl River Estuary and adjacent coastal waters in the wet season using a triply-grid circulation model. *Ocean Model.* **2011**, *38*, 138–162. [[CrossRef](#)]
24. Marchesiello, P.; McWilliams, J.; Shchepetkin, A. Open boundary conditions for long-term integration of regional oceanic models. *Ocean Model.* **2001**, *3*, 1–20. [[CrossRef](#)]
25. Sheng, J.; Greatbatch, R.; Wright, D. Improving the utility of ocean circulation models through adjustment of the momentum balance. *J. Geophys. Res.* **2001**, *106*, 16711–16728. [[CrossRef](#)]
26. Thompson, K.; Ohashi, K.; Sheng, J.; Bobanovic, J.; Ou, J. Suppressing bias and drift of coastal circulation models through the assimilation of seasonal climatologies of temperature and salinity. *Cont. Shelf Res.* **2007**, *27*, 1303–1316. [[CrossRef](#)]
27. Pawlowicz, R.; Beardsley, B.; Lentz, S. Classical tidal harmonic analysis including error estimates in MATLAB using T\_TIDE. *Comput. Geosci.* **2002**, *28*, 929–937. [[CrossRef](#)]
28. Wang, P.; Sheng, J. A comparative study of wave-current interactions over the eastern Canadian shelf under severe weather conditions using a coupled wave-circulation model. *J. Geophys. Res.* **2016**, *121*, 5252–5281. [[CrossRef](#)]
29. Warner, J.; Sherwood, C.; Signell, R.; Harris, C.; Arango, H. Development of a three-dimensional, regional, coupled wave, current, and sediment-transport model. *Comput. Geosci.* **2008**, *34*, 1284–1306. [[CrossRef](#)]
30. Shan, S.; Sheng, J. Examination of circulation, flushing time and dispersion in Halifax Harbour of Nova Scotia. *Water Qual. Res. J. Can.* **2012**, *47*, 353–374. [[CrossRef](#)]
31. Han, G.; Paturi, S.; De Young, B.; Yi, Y.; Shum, C. A 3-D data-assimilative tidal model of the northwest Atlantic. *Atmos. Ocean* **2010**, *48*, 39–57. [[CrossRef](#)]
32. Ohashi, K.; Sheng, J.; Thompson, K.; Hannah, C.; Ritchie, H. Effect of stratification on tidal circulation over the Scotian Shelf and Gulf of St. Lawrence: A numerical study using a three-dimensional shelf circulation model. *Ocean Dyn.* **2009**, *59*, 809. [[CrossRef](#)]
33. Katavouta, A.; Thompson, K.; Lu, Y.; Loder, J. Interaction between the tidal and seasonal variability of the Gulf of Maine and Scotian Shelf region. *J. Phys. Oceanogr.* **2016**, *46*, 3279–3298. [[CrossRef](#)]

34. Zhang, W.; McGillicuddy, D., Jr. Warm spiral streamers over Gulf Stream warm-core rings. *J. Phys. Oceanogr.* **2020**, *50*, 3331–3351. [[CrossRef](#)]
35. Robinson, A.; Glenn, S.; Spall, M.; Walstad, L.; Gardner, G.; Leslie, W. Forecasting Gulf Stream meanders and rings. *EOS Trans. Am. Geophys. Union* **1989**, *70*, 1464–1473. [[CrossRef](#)]
36. Stammer, D.; Wunsch, C. Temporal changes in eddy energy of the oceans. *Deep-Sea Res. II Top. Stud. Oceanogr.* **1999**, *46*, 77–108. [[CrossRef](#)]
37. Gangopadhyay, A.; Gawarkiewicz, G.; Silva, E.; Monim, M.; Clark, J. An observed regime shift in the formation of warm core rings from the Gulf Stream. *Sci. Rep.* **2019**, *9*, 12319. [[CrossRef](#)]
38. Brown, O.; Cornillon, P.; Emmerson, S.; Carle, H. Gulf Stream warm rings: A statistical study of their behavior. *Deep-Sea Res. I Oceanogr. Res. Pap.* **1986**, *33*, 1459–1473. [[CrossRef](#)]
39. Auer, S.J. Five-year climatological survey of the Gulf Stream system and its associated rings. *J. Geophys. Res.* **1987**, *92*, 11709–11726. [[CrossRef](#)]
40. Meneghesso, C.; Seabra, R.; Broitman, B.; Wethey, D.; Burrows, M.; Chan, B.; Lima, F. Remotely-sensed L4 SST underestimates the thermal fingerprint of coastal upwelling. *Remote Sens. Environ.* **2020**, *237*, 111588. [[CrossRef](#)]
41. Ohashi, K.; Sheng, J. Influence of St. Lawrence River discharge on the circulation and hydrography in Canadian Atlantic waters. *Cont. Shelf Res.* **2013**, *58*, 32–49. [[CrossRef](#)]
42. Smith, P.; Schwing, F. Mean circulation and variability on the eastern Canadian continental shelf. *Cont. Shelf Res.* **1991**, *11*, 977–1012. [[CrossRef](#)]
43. Umoh, J.; Thompson, K. Surface heat flux, horizontal advection, and the seasonal evolution of water temperature on the Scotian Shelf. *J. Geophys. Res.* **1994**, *99*, 20403–20416. [[CrossRef](#)]
44. Johnson, C.; Devred, E.; Casault, B.; Head, E.; Spry, J. *Optical, Chemical, and Biological Oceanographic Conditions on the Scotian Shelf and in the Eastern Gulf of Maine in 2016*; Canadian Science Advisory Secretariat (CSAS): Ottawa, ON, Canada, 2018; p. 58.
45. Frantantoni, P.; Pickart, R.; Torres, D.; Scotti, A. Mean structure and dynamics of the shelfbreak jet in the Middle Atlantic Bight during fall and winter. *J. Phys. Ocean.* **2000**, *31*, 2135–2156. [[CrossRef](#)]
46. Loder, J.; Wright, D. Tidal rectification and frontal circulation on the sides of Georges Bank. *J. Mar. Res.* **1985**, *43*, 581–604. [[CrossRef](#)]
47. Tee, K.; Smith, P.; Lefaivre, D. Topographic upwelling off southwest Nova Scotia. *J. Phys. Oceanogr.* **1993**, *23*, 1703–1726. [[CrossRef](#)]
48. Kelly, S.; Lermusiaux, P. Internal-tide interactions with the Gulf Stream and Middle Atlantic Bight shelf break front. *J. Geophys. Res.* **2016**, *121*, 6271–6294. [[CrossRef](#)]
49. Urrego-Blanco, J.; Sheng, J. Formation and distribution of sea ice in the Gulf of St. Lawrence: A process-oriented study using a coupled ocean-ice model. *J. Geophys. Res.* **2014**, *119*, 7099–7122. [[CrossRef](#)]
50. Reeh, N. Greenland ice-sheet mass balance and sea-level change. In *Glaciers, Ice Sheets, and Sea Level: Effect of a CO<sub>2</sub> Induced Climatic Change*; The National Academies Press: Washington, DC, USA, 1985; p. 344.
51. Mertz, G.; Narayanan, S.; Helbig, J. The freshwater transport of the Labrador Current. *Atmos. Ocean* **1993**, *31*, 281–295. [[CrossRef](#)]
52. Thompson, K.; Sheng, J. Subtidal circulation on the Scotian Shelf: Assessing the hindcast skills of a linear, barotropic model. *J. Geophys. Res.* **1997**, *102*, 24987–25003. [[CrossRef](#)]